ALGERIAN DEMOCRATIC AND POPULAR

REPUBLIC

MINISTRY OF HIGH EDUCATATION AND

SCIENTIFIC RESEARCH

Echahid Cheikh Larbi Tebessi University- Tebessa

Faculty of Exact Sciences and Natural and Life Sciences

Department: Material Sciences

Master Thesis

Domain: Material Sciences

SPECIALTY

Materials Physics

THEME

Examining anisothermal effects on dip-coated TiO_2 thin films on glass substrates

By:

BELALA Raounaq

Jury committee:

President:	**HERISSI Labidi**	**Prof.**	**Echahid Cheikh Larbi Tebessi University- Tebessa**
Advisor:	**HANINI Faouzi**	**Prof.**	**Echahid Cheikh Larbi Tebessi University- Tebessa**
Examiner:	**FERDI Abdelhamid**	**M.CA.**	**Echahid Cheikh Larbi Tebessi University- Tebessa**

Defended on: 15/06/2026

Note :..... Mention :.....

ALGERIAN DEMOCRATIC AND POPULAR
REPUBLIC
MINISTRY OF HIGH EDUCATATION AND
SCIENTIFIC RESEARCH
Echahid Cheikh Larbi Tebessi University- Tebessa
Faculty of Exact Sciences and Natural and Life Sciences

Department: Material Sciences

Master Thesis

Domain: Material Sciences
SPECIALTY
Materials Physics

THEME

Examining anisothermal effects on dip-coated TiO_2 thin films on glass substrates

By:

BELALA Raounaq

Jury committee:

President:	**HERISSI Labidi**	**Prof.**	**Echahid Cheikh Larbi Tebessi University- Tebessa**
Advisor:	**HANINI Faouzi**	**Prof.**	**Echahid Cheikh Larbi Tebessi University- Tebessa**
Examiner:	**FERDI Abdelhamid**	**M.CA.**	**Echahid Cheikh Larbi Tebessi University- Tebessa**

Defended on: 15/06/2026

Note :……. Mention :……..……



«يَرْفَعِ اللَّهُ الَّذِينَ آمَنُوا مِنكُمْ وَالَّذِينَ أُوتُوا الْعِلْمَ دَرَجَاتٍ»

المجادلة – الآية 11

ملخص

تم إنتاج أغشية رقيقة من ثاني أكسيد التيتانيوم (TiO_2) بتقنية سول-جل على ركائز زجاجية في درجة حرارة الغرفة. خضعت الأغشية الرقيقة الناتجة للمعالجة الحرارية في نطاق درجة حرارة 300-500 درجة مئوية لمدة ساعة واحدة. استُخدمت تقنيات حيود الأشعة السينية (XRD) ومجهر القوة الذرية (AFM) وقياس طيف الامتصاص الضوئي للأشعة فوق البنفسجية والمرئية لتحليل الخصائص الفيزيائية لأغشية TiO_2 المنتجة. كشفت النتائج أن الأغشية النامية غير متبلورة، وأنها تتحول جزئيًا إلى طور الأناتاز بعد المعالجة الحرارية عند 500 درجة مئوية. تُظهر القياسات البصرية أن الأغشية شفافة في نطاق الضوء المرئي، مع وجود فجوة طاقة تضيق مع ارتفاع درجة حرارة التلدين. ويُبين تحليل المجهر الذري للقوة (AFM) زيادة في خشونة سطح أغشية ثاني أكسيد التيتانيوم (TiO_2) بعد التلدين. وقد وُجد أن قيم فجوة الطاقة البصرية تتراوح بين 3.21 و3.62 إلكترون فولت، وفي نفس الوقت يزيد الاضطراب، مما يشير إلى أن عملية التلدين تؤثر بشكل ملحوظ على الخصائص التركيبية والبصرية لأغشية ثاني أكسيد التيتانيوم الرقيقة.

الكلمات المفتاحية: ثاني أكسيد التيتانيوم، طريقة سول-جل، التلدين، حيود الأشعة السينية، فجوة الطاقة البصرية ، مجهر القوة الذرية.

Abstract

TiO_2 thin films have been produced by sol-gel technique on glass substrates at ambient temperature. The resultant thin films have been annealed in the temperature range 300-500°C for 1 hour. X-ray diffraction (XRD), atomic force microscopy (AFM) and UV–vis transmission spectrophotometry techniques have been applied to analyze the physical properties of the produced TiO_2 films. The results reveal that the as grown films are amorphous and are partially converted into anatase phase following annealing at 500°C. The optical measurements demonstrate that the films are transparent in the visible region with the existence of a band gap narrowing with increasing annealing temperature. The atomic force microscopy (AFM) analysis demonstrates an increase in the surface roughness of the TiO_2 films after annealing. The values of the optical band gap were found to vary between 3.21 to 3.62 eV and at the same time the disorder increases, thus indicating that the annealing procedure considerably impacts the structural and optical properties of the TiO_2 thin films.

Keywords: TiO_2, Sol-gel, Annealing, XRD, Optical band gap, AFM.

Résumé

Des couches minces de TiO_2 ont été élaborées par la technique sol-gel sur des substrats de verre à température ambiante. Les couches minces obtenues ont ensuite été recuites pendant une heure à des températures comprises entre 300 et 500 °C. Les propriétés physiques des couches de TiO_2 ont été analysées par diffraction des rayons X (DRX), microscopie à force atomique (AFM) et spectrophotométrie de transmission UV-visible. Les résultats montrent que les couches initiales sont amorphes et qu'elles se transforment partiellement en phase anatase après recuit à 500 °C. Les mesures optiques démontrent que les films sont transparents dans le visible, avec un rétrécissement de la bande interdite lorsque la température de recuit augmente. L'analyse par microscopie à force atomique (AFM) révèle une augmentation de la rugosité de surface des films de TiO_2 après recuit. Les valeurs de la bande interdite optique varient entre 3,21 et 3,62 eV, et en même temps le désordre augmente, ce qui indique que le recuit influence considérablement les propriétés structurales et optiques des films minces de TiO_2.

Mots-clés : TiO_2, sol-gel, recuit, DRX, La bande interdite optique, AFM.

Acknowledgements

*First and foremost, we are grateful to « **ALLAH** », the Almighty, for giving us the patience, bravery, and faith to complete this task. Then, we pray to Allah to facilitate our scientific endeavors and grant us the knowledge to aid others and advance humankind.*

This work was carried out at the Echahid Cheikh Larbi University Tébessi-Tébessa's Applied and Theoretical Physics Laboratory.

*I would like to thank **Pr. HANINI FAOUZI** professor at the Echahid Cheikh Larbi University Tébessi-Tébessa's Department of Material Sciences, Faculty of Exact Sciences and Natural and Life Sciences, for allowing us to work under his direction as our academic supervisor, as well as for his insightful advice and ideas, all of which were very helpful to us while we conducted research for our master's thesis.*

*I also want to express our gratitude to the evaluation committee members **Pr. HERISSI LABIDI** and **Dr. FERDI ABDELHAMID** who honored us by agreeing to review and improve this work.*

Finally, but just as importantly, we want to express our gratitude to our loving parents, relatives, and friends for their encouragement and support.

DEDICATION

To my parent,

To my self,

To my brothers ,

To my sisters .

Raounaq

TABLE OF CONTENTS

TABLE OF CONTENTS

ملخص		I
ABSTRACT		II
RESUME		III
ACKNOWLEDGEMENT		IV
DEDICATION		V
DEDICATION		VI
TABLE OF CONTENTS		VII
LIST OF TABLES		VIII
LIST OF FIGURES		IX
GENERAL INTRODUCTION		X
	Chapter I: Literature Review	
I.1	Thin films concept	3
	I.1.1.Mechanism of Thin Films Formation	3
	I.1.2. Thin film growth modes	5
I.2	Classification of thin films deposition techniques	6
	I.2.1. Physical vapor deposition (PVD)	6
	I.2.1.1. Electron beam evaporation	7
	I.2.1.2. Vacuum thermal evaporation technique	8
	I.2.1.3. Pulsed laser deposition (PLD)	9
	I.2.2. Chemical vapour deposition (CVD)	10
	I.2.2.1. Spray Pyrolysis technique	10
	I.2.2.2. Sol-gel technique	11
	I.2.2.3. Sol-gel process	11
	I.2.2.4. Hydrolysis and condensation	12
	I.2.2.5.The sol-gel transition	12
	I.2.2.6. Different sol-gel technique	13
I.3	Titanium dioxide (TiO_2)	15
	I.3.1. Structural properties	16
	I.3.2. Stability of crystalline phases	17
	I.3.3. Optical properties	17
	I.3.4. Electrical Properties	18
	I.3.5. Titanium dioxide applications	19

I.3.6. Effect of annealing temperature 21

Chapitre II : Elaboration technique and characterization Tools

II.1 Preparation of the substrate 22
II.1.1. Choice of substrate 22
II.1.2. Cleaning of the substrate 22
II.2 Preparation of the sol for TiO_2 thin film fabrication 23
II.3 Deposition setup (dip-coating) 23
II.4 The annealing or heat treatment 26
II.5. Characterization techniques of thin films 26
II.5.1. Structural characterization with X-ray diffraction 26
II.5.2. Atomic Force Microscopy (AFM) 28
II.5.3. Optical characterization and measurement 30

Chapitre III : Experimental results and discussion

III.1 Structural Studies 35
III.1.1. XRD analysis 35
III.2 Surface morphology analysis by AFM 36
III.3 Optical properties 38
III.3.1. UV–vis analysis 38
III.3.2. Band gap and Urbach energy 40
CONCLUSION 44
REFERENCES 46

LIST OF TABLES

Table.I.1	Classification of thin film deposition technique	**06**
Table.I.2	Crystal structure data of TiO_2	**15**
Table.II.1	Different reagents used for the preparation of TiO2 thin films by sol-gel	**23**

LIST OF FIGURES

Figure.I.1	Sequential stages of silver thin film deposition on molybdenum disulfide (MoS_2)	**04**
Figure.I.2	Schematic diagram of three basic growth modes	**05**
Figure.I.3	Operating principle of electron beam evaporation	**07**
Figure.I.4	Illustrating the schematic of thermal evaporation by resistive heating	**08**
Figure.I.5	General diagram of PLD	**09**
Figure.I.6	Schematic diagram of the spraying system	**10**
Figure.I.7	Sol-gel process	**11**
Figure.I.8	Evolution of the viscosity of the solution and of the elastic constant of the gel	**13**
Figure.I.9	The four steps of spin coating	**14**
Figure.I.10	Dip-coating stages	**14**
Figure.I.11	Crystal structure of anatase, rutile and brookite	**16**
Figure.I.12	TiO_2 band structure for rutile, anatase and brookite	**18**
Figure.I.13	General mechanism of photo-catalysis	**20**
Figure.II.1	Photo of the glass substrate used	**22**
Figure.II.2	Experimental layer drawing device used at the Thin Films and Interfaces Laboratory of Constantine 1 University	**23**

Figure.II.3	Schematic flowchart for the preparation of TiO_2 thin films	**25**
Figure.II.4	A photograph of the TiO_2 samples as a function of the annealing temperature for TiO2 films.	**26**
Figure.II.5	Principle of XRD	**27**
Figure.II.6	Basic features of a typical XRD experiment	**27**
Figure.II.7	Definition of β from the diffraction curves	**28**
Figure.II.8	Schematic diagram of Atomic Force Microscope (AFM)	**29**
Figure.II.9	Schematic representation of UV-Visible Spectrophotometer	**31**
Figure.II.10	Interference fringes used for film thickness determination	**32**
Figure.II.11	Determination of optical band gap	**33**
Figure.II.12	Determination of Urbach energy	**34**
Figure.III.1	X-ray diffraction patterns of thin TiO_2 films on glass substrates	**35**
Figure.III.2	2D AFM images of TiO_2 films	**36**
Figure.III.3	RMS roughness of TiO_2 thin films as a function of annealing temperature	**37**
Figure.III.4	UV–vis transmittance spectra of TiO_2 films	**38**
Figure.III.5	(a) Average optical transmission at 633 nm vs annealing temperature (b) Correlation between surface roughness and visible transmittance vs annealing temperature	**39**
Figure.III.6	Optical absorption spectra $(\alpha h\nu)^{1/2}$ versus energy $(h\nu)$	**40**
Figure.III.7	Variation of ln (α) as a function of hν in TiO2 thin films	**42**
Figure.III.8	Variations in the gap and disorder as a function of the annealing temperature for TiO_2 films	**42**

Introduction

One of the most essential and adaptable functional materials for high definition optical display systems and next generation optoelectronic technologies working in the ultraviolet (UV) band is titanium dioxide (TiO_2) .TiO_2 thin films are now essential components of many cutting-edge industrial applications because of their remarkable chemical stability, high refractive index, and non-toxic nature .

These include energy-harvesting dye-sensitized solar cells (DSSCs), high-sensitivity solid-state gas sensors, smart electrochromic windows, high-efficiency anti-reflection coatings, and photocatalytic environmental cleanup. Optimizing the deposition characteristics of these thin films has received significant funding over the last ten years from a coordinated worldwide research effort. At the same time, surfactant-assisted self-assembly has become a very popular method for creating highly organized, mesoporous TiO_2 structures. By improving a number of scalable chemical techniques, including

Anatase, rutile, and brookite are the three primary natural crystal forms of titanium dioxide (TiO_2). Anatase and rutile are two of them that are crucial for the production of optical and electrical devices. Anatase is still the best option for optical guides and light-driven chemical processes (photocatalysis), despite having a greater energy band gap (3.2 eV) than rutile (3.0 eV). This is due to the fact that it efficiently absorbs UV rays and allows light to flow through it nicely from visible to infrared. Furthermore, by baking thin TiO_2 coatings, producers can readily modify their structure. The coatings are initially disorganized (amorphous), but heating them results in a long-lasting transformation: first, they become anatase, then as the temperature rises, they become rutile.

The current work focuses on the production of TiO_2 thin films using titanium isopropoxide as the main precursor and a sol-gel dip-coating technique. Analyzing how the annealing temperature affects the final films' structural, morphological, and optical properties is given particular attention.

This study is divided into three chapters, in addition to the introduction and conclusion.

- A brief introduction to thin films is given in ***Chapter I***, which then focuses on the Sol-Gel procedure that we employed to develop our thin films. Additionally, a bibliographic analysis about the different characteristics of TiO_2 and their applications is provided in this regard.

- A thorough description of the numerous steps involved in the development of our thin films utilizing the Sol-Gel technology is provided in **Chapter II**, along with a variety of approaches and characterization tools,

- Lastly, the experimental results and their interpretations pertaining to the samples made using the Sol-Gel process are described in the **final chapter**.

Chapter I

Literature Review

I.1. Thin films concept

A thin film is a material deposited on a substrate and characterized by a substantially reduced thickness, typically ranging from a few nanometers (nm) to several micrometers (μm) [1, 2]. Owing to this reduced dimension, the film exhibits a quasi-two-dimensional nature, which can significantly modify many of its physical properties compared with those of the bulk material [3]. Thin films, therefore, differ from bulk materials not only in thickness but also in their microstructure, geometry, and surface-related behavior. The fundamental distinction between a material in its bulk form and in its thin film state lies in the increasing importance of surface and interface effects. In bulk materials, the influence of boundaries is generally negligible, whereas in thin films, surface-related phenomena may become predominant and strongly affect the material properties. However, when the film thickness exceeds a certain critical threshold, size-related effects gradually diminish, and the material tends to recover the well-established properties of the bulk state [4].

I.1.1. Mechanism of Thin Films Formation

Thin films are applied to a substrate through thermal evaporation, chemical decomposition, and/or the evaporation of source materials via the irradiation of energetic species or photons. Any thin-film deposition procedure comprises three primary stages [5]:

- Generation of the requisite atomic, molecular, or ionic entities,
- Conveyance of these species to the substrate,
- Condensation on the substrate, either directly or through a chemical and/or electrochemical reaction, resulting in the formation of a solid deposit.

The unit species, when contacting the substrate, lose their velocity component perpendicular to the substrate (assuming the incoming energy is not excessively high) and are physically adsorbed onto the substrate surface. The adsorbed species are not immediately in thermal equilibrium with the substrate and migrate over the substrate surface. During this process, they engage with one another, generating larger clusters [5].

The clusters, referred to as nuclei, are thermodynamically unstable and may desorb over time, contingent upon the deposition conditions. If the deposition settings allow a cluster to interact with other adsorbed species prior to desorption, it begins to increase in size. Upon attaining a specific critical size, the cluster attains thermodynamic stability.The system is stable, and the nucleation barrier is considered to have been surmounted. The process of forming stable, chemisorbed, critical-sized nuclei is referred to as the nucleation stage [6].

The essential nuclei increase in both quantity and size until reaching a saturation nucleation density. The nucleation density and average nucleus size are influenced by various characteristics, including the energy of the impinging species; the impingement rate; the activation energies for adsorption, desorption, and thermal diffusion; as well as the substrate's temperature, topography, and chemical composition. A nucleus can expand both parallel to the substrate through surface diffusion of the adsorbed species and perpendicular to it via direct impingement of the incident species. Generally, the rate of lateral expansion at this stage significantly exceeds that of perpendicular growth. The developed nuclei are referred to as islands [7]. The evolution of thin-film growth from isolated nuclei to a continuous layer is schematically illustrated in Figure I.1.

The subsequent phase in the film generation process is the coalescence stage, during which the small islands merge to minimize the substrate surface area. This inclination to create larger islands is referred to as agglomeration and is facilitated by augmenting the surface mobility of the adsorbed species. Expansive islands amalgamate, resulting in channels and depressions of exposed substrate. The films' structure at this stage transitions from a discontinuous island type to a porous network type. The filling of channels and holes creates a wholly continuous film [6, 7].

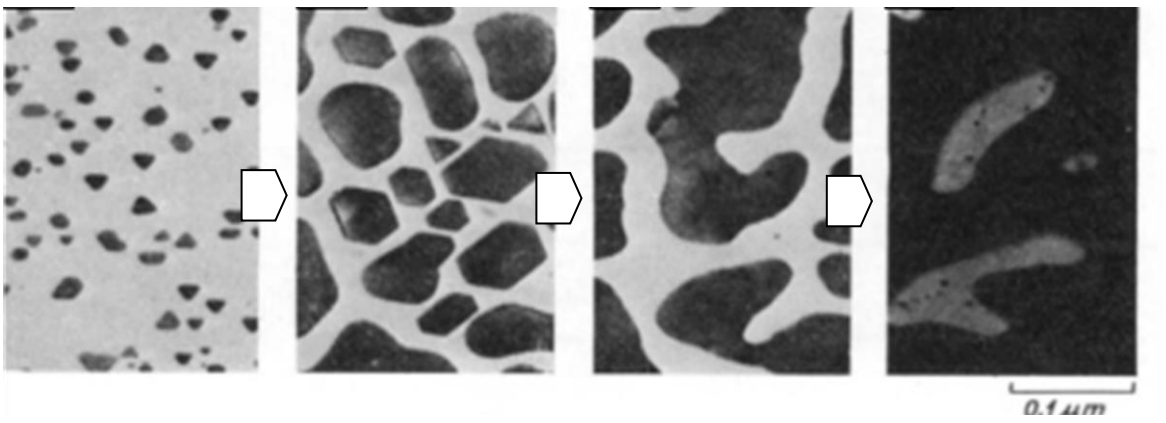


Figure I.1. Sequential stages of silver thin film deposition on molybdenum disulfide (MoS_2) [8].

I.1.2. Thin film growth modes

The effective surface free energy can be characterized by interfacial energies, γ_{SV}(substrate-vacuum), γ_{AV} (adsorbate-vacuum) and γ_{SA} (substrate-adsorbate). Based on the sign and magnitude of the resulting energy balance, the thin film growth mode can be predicted as shown in Figure I.2 [9, 10]:

$$\Delta_\gamma = \gamma_{AV} + \gamma_{SA} - \gamma_{SV} \quad \text{(I.1)}$$

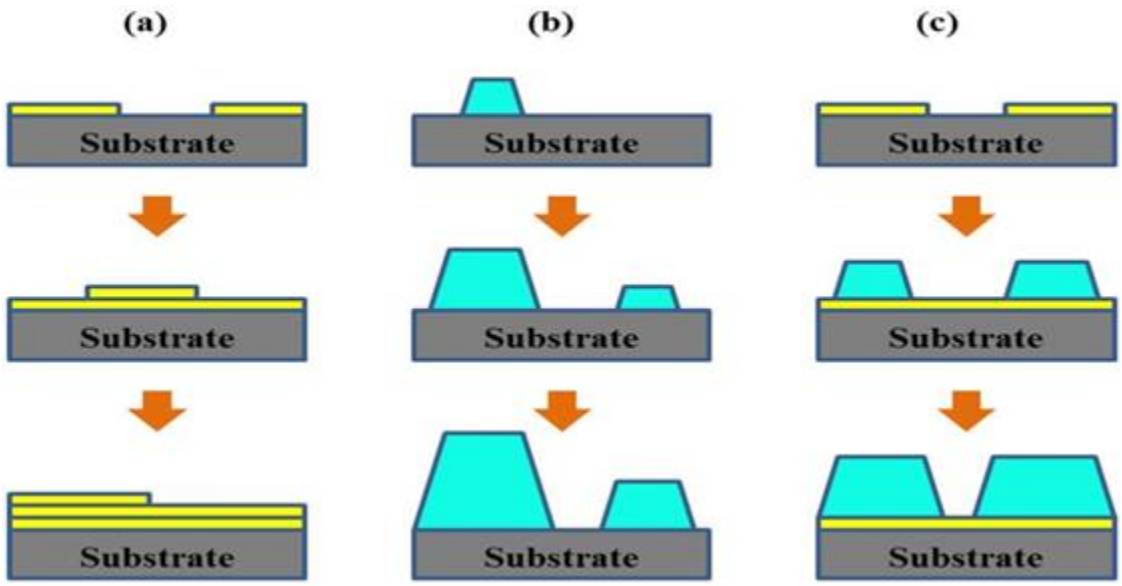


Figure I.2. Schematic diagram of three basic growth modes [10].

a) Volmer-Weber growth

Negative values of Δ_γ imply stronger cohesive interactions between adsorbate atoms than adhesive ones between adsorbate and substrate. The deposited species tend to agglomerate, resulting in the creation of three-dimensional islands. Sometimes it is called 'island growth'. In rare situations, the coalescence of islands might ultimately produce smooth granular films [9, 10].

b) Frank-van der Merwe growth

The growth mode (also called layer-by-layer growth) occurs when $\Delta_\gamma > 0$, i.e., the adsorption on the substrate is energetically favourable. The film grows first in a perfect monolayer and then in further layers one after the other. In this regime, the adatoms tend to occupy the energetically stable adsorption sites, leading to the two-dimensional growth mode [10].

c) Stranski-Krastanov growth

The Stranski-Krastanov mechanism is an intermediate growth mode in which one or multiple initial monolayers are generated in a layer-by-layer manner and then followed by the nucleation of three-dimensional islands. Such behavior is generally observed when the surface energy balance is close to equilibrium ($\Delta_\gamma = 0$) and is impacted by strain effects and lattice mismatch [10].

I.2. Classification of thin films deposition techniques

The thin film materials are obtained by different ways of deposition; deposition methods are roughly divided in two categories, chemical vapor deposition (CVD) and physical vapor deposition (PVD) (Table I.1).

Table I.1. Classification of thin film deposition technique.

PVD	CVD
1. Vacuum : ✓ Evaporation technique ✓ Pulsed laser deposition	1. Solution : ✓ **Sol-gel** ✓ Electro-deposition ✓ Spray pyrolysis
2. Plasma : ✓ Sputtering (DC/RF)	2. Gas : ✓ CVD

I.2.1. Physical vapor deposition (PVD)

PVD refers to a group of thin film deposition techniques in which a solid material is vaporised and then condensed onto a substrate under vacuum or low pressure conditions [11, 12]. This process acts on an atomic scale. The atoms, molecules or ions are generated in a vacuum or plasma environment and transported towards the substrate. Upon arrival, these species are adsorbed and nucleate and grow to form a thin film.

In many PVD systems the vapor phase may consist of ionized species or plasma, which can have a significant effect on the kinetics of film growth and the resulting microstructure. Furthermore, when a reactive gas is introduced into the chamber and chemical reactions take place either in the vapor phase or at the substrate surface, the process is called reactive deposition, which allows the formation of compound thin films. In general, PVD techniques allow the deposition of thin films with a thickness from a few nanometres to some micrometres depending on the working conditions and applications [13, 14].

I.2.1.1. Electron beam evaporation (EBE)

In EBE, a stream of electrons is accelerated by electric fields typically ranging from 5 to 10 kV and directed onto the surface of the material for the purpose of evaporation. The electrons rapidly dissipate their energy upon impact with the surface, causing the material to melt at that location vaporises. The surface is heated directly by impinging electrons, unlike conventional heating methods. Direct heating facilitates the evaporation of substances from water-cooled crucibles. Water-cooled crucibles are essential for the evaporation of reactive, particularly refractory, materials to minimise interactions with the crucible walls. This facilitates the production of high-purity films by almost eliminating the evaporation of crucible materials or their reaction products [15, 16].

Electron beam sources are categorised into thermionic and plasma electron sources.

In the thermionic configuration, electrons are produced from heated refractory metal filaments, rods, or discs. In the plasma configuration, the electron beam is extracted from a confined plasma region [17]. Figure I.3 shows the experimental setup of the EBE system.

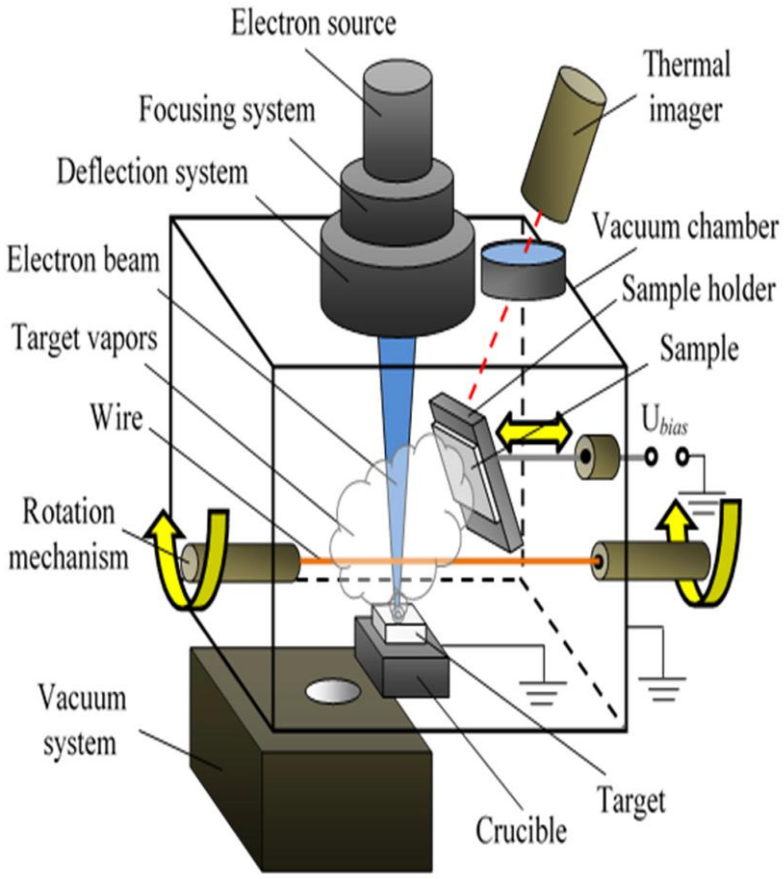


Figure I.3. Operating principle of electron beam evaporation [18].

I.2.1.2. Vacuum thermal evaporation technique

Thermal evaporation is the predominant method for fabricating thin films of metals, alloys, and other compounds due to its simplicity and convenience. The sole criterion is to maintain a vacuum atmosphere while providing an adequate amount of heat. The heat must be applied to the evaporants to achieve the requisite vapor pressure for evaporation. The vaporised substance is allowed to condense on a substrate maintained at an appropriate temperature as shown in Figure I.4. Evaporation in a vacuum significantly reduces the evaporation temperature and minimises the development of oxides and the integration of contaminants in the developing layer. Evaporation typically occurs at a pressure of 10^{-5} Torr. At this pressure, a linear trajectory for the majority of the ejected vapor atoms is guaranteed, with a substrate-to-source distance of approximately 10 to 50 cm [19]. The attributes and quality of the deposited film are contingent upon substrate temperature, deposition rate, ambient pressure, and other factors, while film uniformity is influenced by the geometry of the evaporation source and its distance from the substrate. Thermal evaporation deposition is straightforward, convenient, and extensively utilized [20].

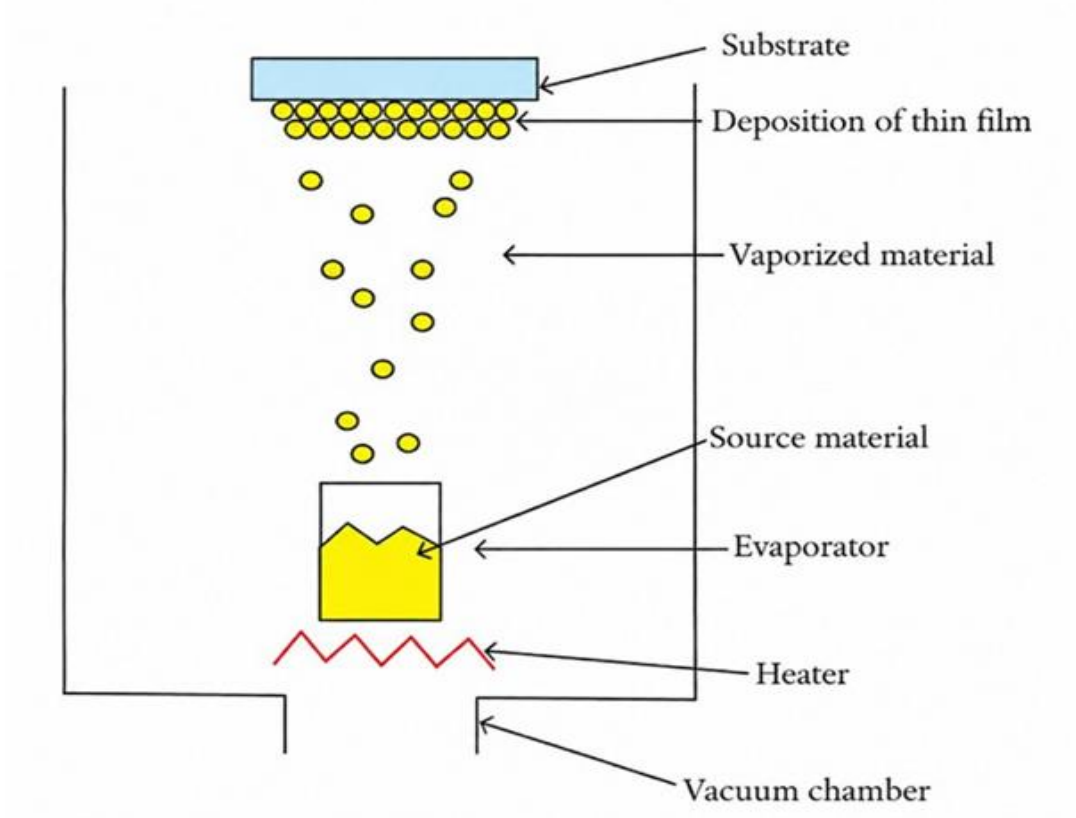


Figure I.4. Illustrating the schematic of thermal evaporation by resistive heating [21].

I.2.1.3. Pulsed laser deposition (PLD)

The basic concept behind this technique, called pulsed laser deposition Figure I.5, is quite simple. A solid target material inside an ultra-high vacuum chamber is irradiated by a pulsed laser beam. Under appropriate interaction conditions, material is ablated and deposited onto a substrate positioned opposite to the target. Many parameters influence the quality and properties of the deposited films. It is always necessary to control the dynamics of the ablated species from the target to the substrate.

There are several key characteristics associated with the deposition process by laser ablation:

- Stoichiometric transfer of the target material's substance to the substrate facilitates the deposition of complex materials, such as high-temperature superconductors.
- Film purity depends mainly on target purity, as well as vacuum conditions and background gas.
- The main requirement for deposition is that the material must absorb the laser wavelength.

When ultrashort laser pulses are used, it is possible to attain much greater power densities with pulse duration in the femtosecond range (10^{-15} s). Then, the laser–matter interaction differs significantly between femtosecond pulses and nanosecond pulses. There are highly energetic species, present in the plasma, that reach KeV energy levels. These energetic species enhance film adhesion [22].

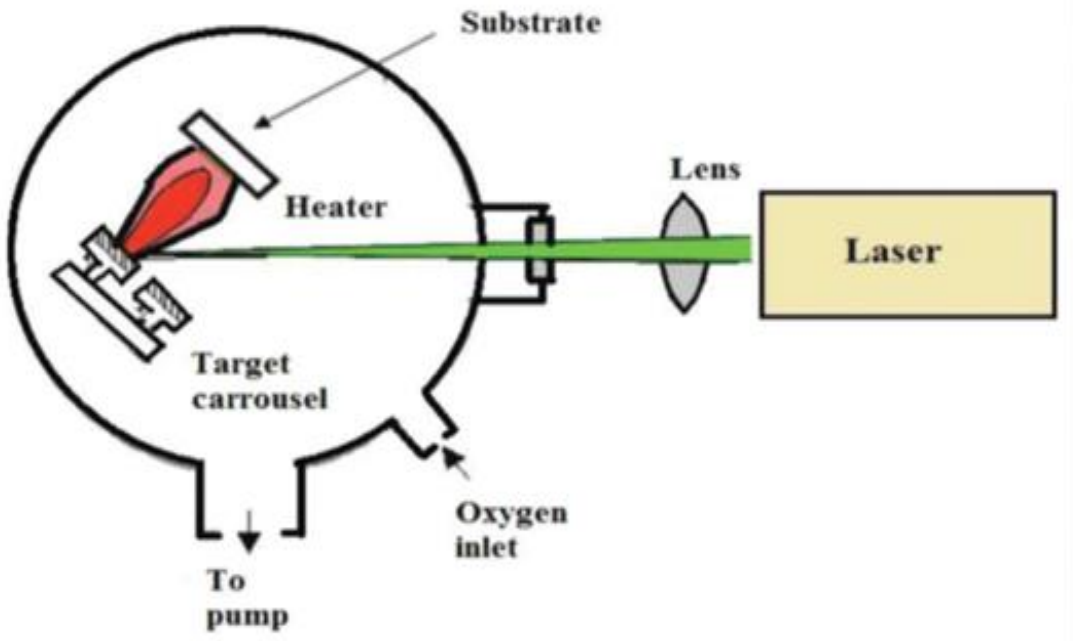


Figure I.5. General diagram of PLD [23].

I.2.2. Chemical vapour deposition (CVD)

CVD is a general term for the deposition of a thin layer via a sequence of chemical reactions. Material synthesis involves a chemical reaction between the target constituent in the vapour phase and the substrate's surface, resulting in the formation of a thin coating. It should be noted that the mechanics underlying CVD differ significantly from those used in PVD. PVD produces thin films by condensing atoms or molecules on the substrate's surface through evaporation, ion bombardment, or sputtering [24, 26]. CVD is a complex thermodynamic process that involves chemical reactions under specified parameters including temperature, pressure, reaction rates, momentum, mass, and energy transmission. CVD film quality is influenced by various process parameters such as flow rates, pressure, temperature, chemical species concentration, and reactor geometry [27, 28].

I.2.2.1. Spray Pyrolysis technique

Spray pyrolysis Figure I.6 is a cost-effective and easy technology that uses the chemical vapour deposition CVD process. This process involves spraying a solution of the substance to be deposited onto a heated substrate, utilising air as a carrier gas [29]. Spray pyrolysis involves several deposition variables, including substrate temperature, gas and solution flow rates, precursor concentration, deposition period, and substrate-nozzle distance. Some of these characteristics depend on one another. To analyse the consequences of any one of these, the others must remain constant [30].

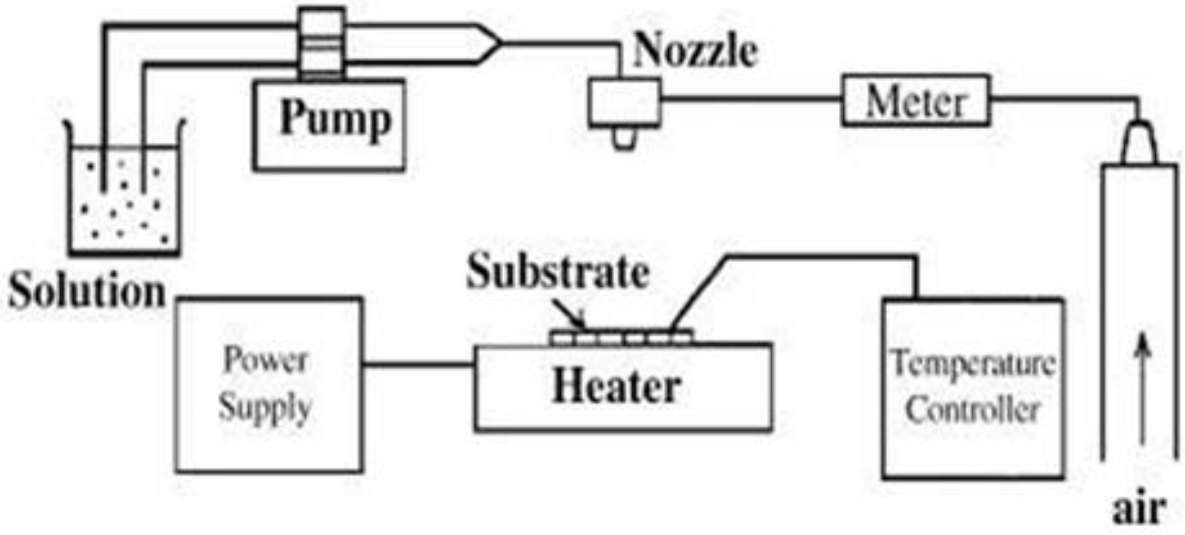


Figure I.6. Schematic diagram of the spraying system [29].

I.2.2.2. Sol-gel technique

The sol-gel method is a chemical deposition technique that involves transforming a liquid into a gel and then heating it to form a solid oxide material [31]. This method may be used to create fibres, ceramics, thin films, and powders. It is very effective for creating thin oxide layers for coatings [32]. Because of its wide range of materials and formatting options, this approach has become popular in sectors such as optics, electronics, photochemistry, and biomaterials. It also offers the advantage of using soft chemistry, which can result in extremely pure and stoichiometric materials. From a technological standpoint, films are particularly significant [31, 33].

I.2.2.3. Sol-gel process

The sol-gel technique converts a liquid (colloidal solution) to a gel phase. Inorganic metal salts or metal-organic compounds, such as metal alkoxide, are commonly utilised as precursors. Precursors undergo hydrolysis and condensation reactions to generate a colloidal suspension (sol). The sol particles then condense, forming a continuous liquid phase (gel) [34]. The sol-gel method involves three reactions Figure I.7: hydrolysis, alcohol condensation, and water condensation. Because water and alkoxides are immiscible, alcohol is frequently utilised as a cosolvent [22].

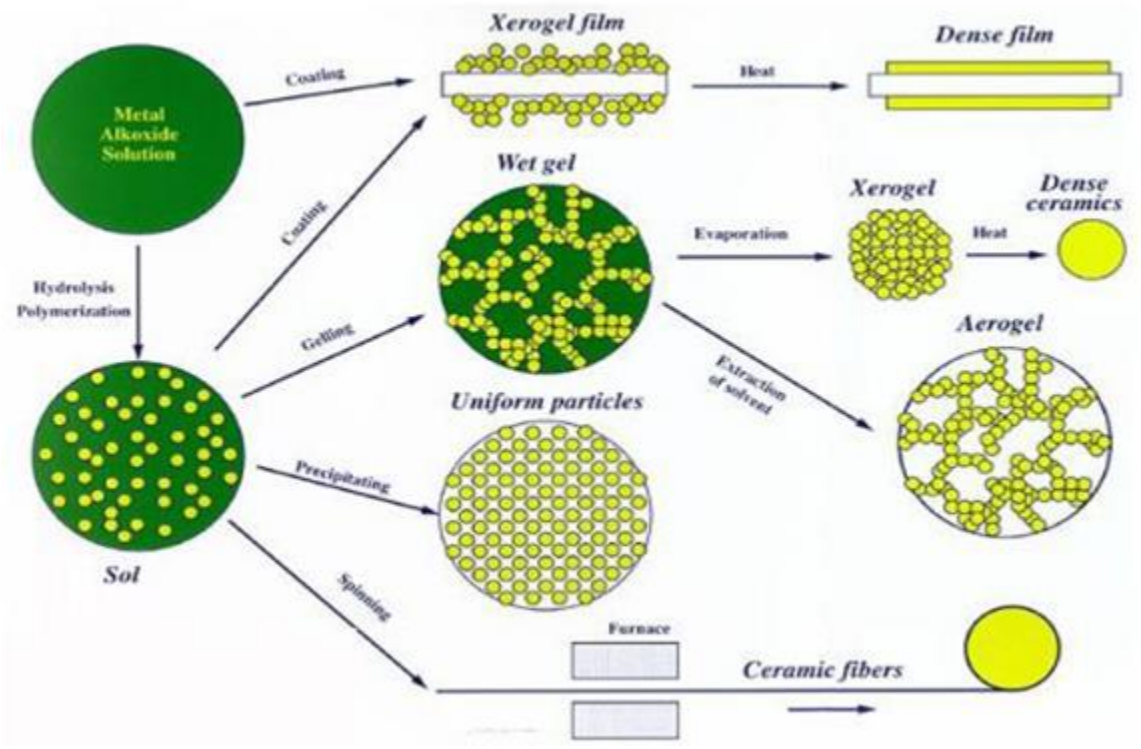


Figure I.7. Sol-gel process [35].

I.2.2.4. Hydrolysis and condensation

✓ Hydrolysis

The hydrolysis reaction involves replacing alkoxide groups (OR) with hydroxyl groups (OH) by adding water, as shown in the equation below.

$$M(OR)_n + xH_2O \rightarrow M(OR)_{n-x} - (OH)_x + x\,ROH \quad (I.2)$$

The hydrolysis reaction is characterised by the consumption of water and the release of alcohol. Following this stage, the precursors are functional in relation to the condensation step [36].

✓ Condensation

Condensation reactions start with the emergence of hydroxyl groups and result in the production of bonds or metalloxane bridges (M-O-M). The condensation reaction can occur between various groups.

- Oxolation occurs when the groups (OH-M-(OR) $_{n-1}$) react, resulting in a water molecule. In this context, "OH" refers to a hydroxyl group, which consists of an oxygen atom bonded to a hydrogen atom. The reaction is expressed as:

$$\mathrm{M(OH)_n(OR)_x(OR)_{n-y} + M(OH)_2 \leftrightarrow (OR)_{n-x}(OH)_{x-1}M - O - M(OR)_{y-1} + (OR)_{n-x} + H_2O} \quad (I.3)$$

- Alkoxolation occurs when the groups (OH-M-(OR) $_{n-1}$) combine with non-hydrolysed groups MOR, resulting in the alcohol molecule R-OH.

$$(OR)_{n-x}M(OH)_n + M(OR)_n \leftrightarrow (OR)_{n-x}\,(OH)_{n-x}M - O - M(OR)_{n-1} + ROH \quad (I.4)$$

The condensation reaction is linked to hydrolysis; therefore, the parameters affecting hydrolysis also impact the condensation reaction's mechanism and kinetics, ultimately affecting the gel's properties [36].

I.2.2.5.The sol-gel transition

Gelation often occurs when polymer chains expand and clump together due to condensation. As the hydrolysis and condensation events occur, polymer clusters grow in size. The sol-gel transition point occurs when one of the clusters achieves an infinite dimension, resulting in an infinite viscosity. The "gel fraction" continues to expand and incorporate smaller polymeric units. When all bonds are utilized, the gel is created. Macroscopically, the solution's mechanical behavior can indicate the transition. Such behavior causes the solution's viscosity to diverge and increases the elastic constant in gel phase G (or Coulomb's modulus) [37].

Figure I.8 depicts the mechanical behavior of the solution by tracking the change of soil viscosity and coulomb modulus G (elastic constant) over time. When the gel is fully produced, the viscosity becomes infinite and the constant G approaches its maximum value. Thermal heating eliminates the trapped liquid masses in this structure [36].

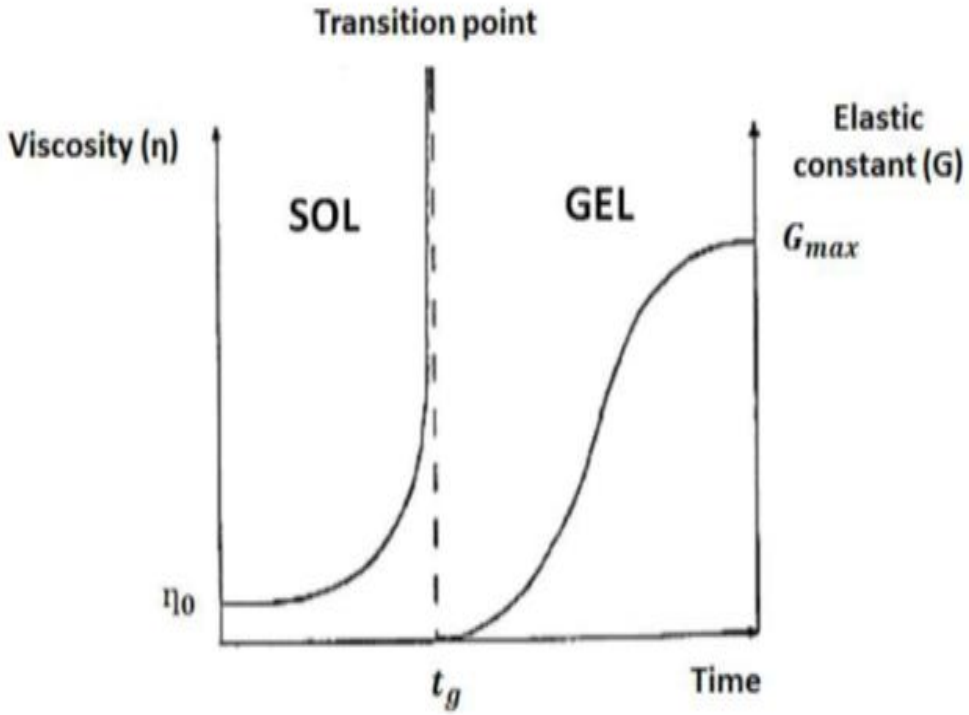
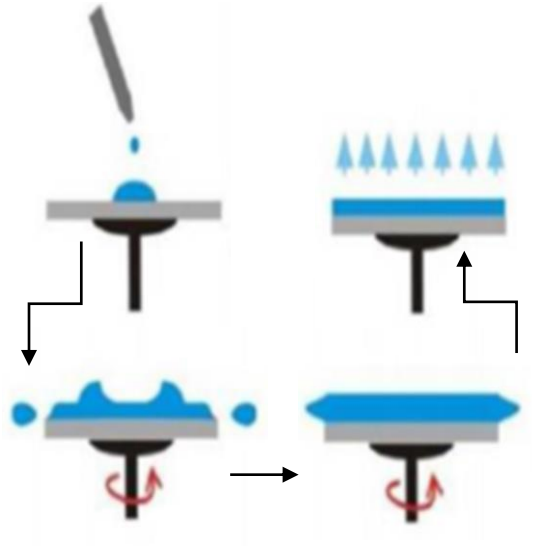


Figure I.8. Evolution of the viscosity of the solution and of the elastic constant of the gel [37].

I.2.2.6. Different sol-gel technique

Thin film deposition on a substrate can be done using many ways, i.e., spin-coating, drain-coating, and dip-coating. Each substrate has unique features that influence the manner of deposition, such as its geometry, size, and surface energy, which can affect adhesion and film uniformity. Geometry or size. The two methods described here are the most widely employed [5].

Spin coating: To use this procedure, apply a small amount of fluid resin to the center of a substrate. The substrate is then spun at high speeds. This strategy is cost-effective and easy to execute. It produces great results on planar substrates with diameters of cm^2. Figure I.9 illustrates the four phases of the deposition process.



1) Deposition of the solution. 2) The start of rotation: the acceleration step forces the liquid to flow outward from the substrate. 3) By rotating at a steady speed, extra liquid can be ejected in the form of droplets. a consistent drop in film thickness. 4) Evaporation of the volatile solvent reduces the thickness of the deposited coating [39]. Final film thickness and other properties depend on the parameters chosen for the spin process.

Figure I.9. The four steps of spin coating [38].

Dip coating: Dip coating involves evaporating the solvent from a polymer solution to form a film. To create a solid polymer film on a substrate, dip it into a polymer solution, remove it at a steady speed, and let the solvent evaporate. Scriven et al. [40] separated the dip coating process into five stages: immersion, start-up, deposition, drainage, and evaporation, as illustrated in Figure I.10.

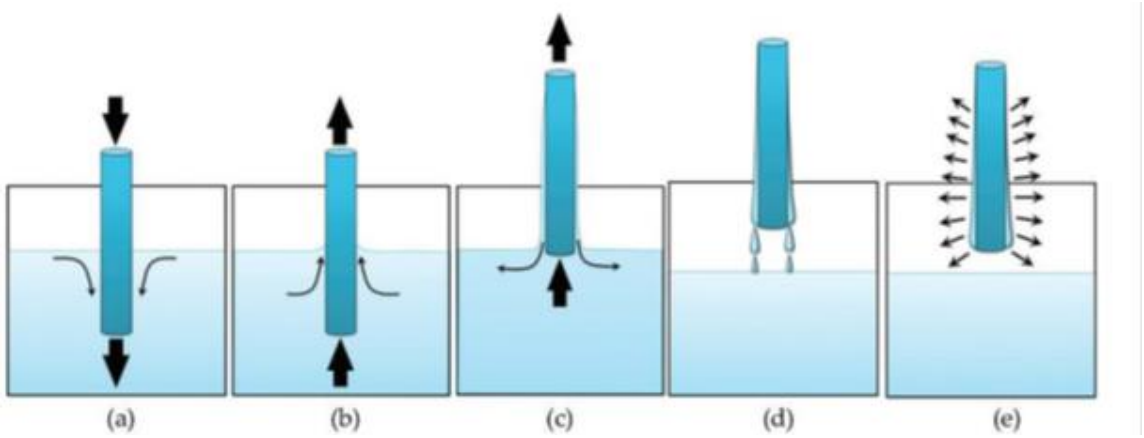


Figure I.10. Dip-coating stages [42].

The thickness of the coating layer is dependent on the following factors [39]: (1) the speed with which the substrate is removed; (2) the solution's concentration; (3) the solution's viscosity; (4) the rate at which the solvent evaporates; (5) the angle at which the substrate is extracted; (6) the solution's surface tension; (7) vapor pressure; (8) maintaining temperature and humidity levels above the coating bath; and (9) controlling air velocity, substrate, and solution temperatures precisely.

The thickness of the deposited film depends on the position of the streamline that separates the upward and downward flowing layers. The film deposition region is influenced by five forces: viscous drag from the moving substrate, gravity, surface tension in the concave meniscus, inertial force from the boundary layer liquid, and surface tension gradient [41].

I.3. Titanium dioxide (TiO_2)

Titanium was discovered in 1791 by William Gregor, a British priest and mineralogist, while analysing black magnetic sands from Menachan, Cornwall [43]. Titanium is a strong and light metal with high strength and low density. However, it is difficult to obtain in its pure state due to its affinity for oxygen, carbon, and nitrogen. Titanium undergoes passivation, which is the process of making a material passive by depositing an oxide layer on its surface [44]. Titanium dioxide was discovered in the early 1900s, and its usage as a pigment (anatase form) began in 1923 in France. It eventually superseded lithopone and poisonous lead-based pigments in the early 1930s. TiO_2 is found in three crystalline structures: rutile, anatase, and brookite [45]. The detailed crystallographic parameters for each phase, including space group and lattice constants, are summarized in Table I.2. The crystal structures of anatase, rutile, and brookite are illustrated in Figure I.11.

Table I. 2.Crystal structure data of TiO_2 [49].

Phase	Rutile	Anatase	Brookite
Crystal structure	Tetragonal	Tetragonal	Orthorhombic
Lattice constants (Å)	a=4.5936 c=2.9587	a=3.784 c=9.515	a=9.184 b=5.447 c=5.145
Molecules/cell	2	4	8
Volume/molecule ($Å^3$)	31.2160	34.061	32.172
Density (g/cm^3)	4.13	3.79	3.99
***Ti–O* bond length (Å)**	1.949 (4) 1.980 (2)	1.937 (4) 1.965 (2)	1.87~2.04
***O–Ti–O* bond angle**	81.2° 90°	77.7° 92.6°	77°□105°

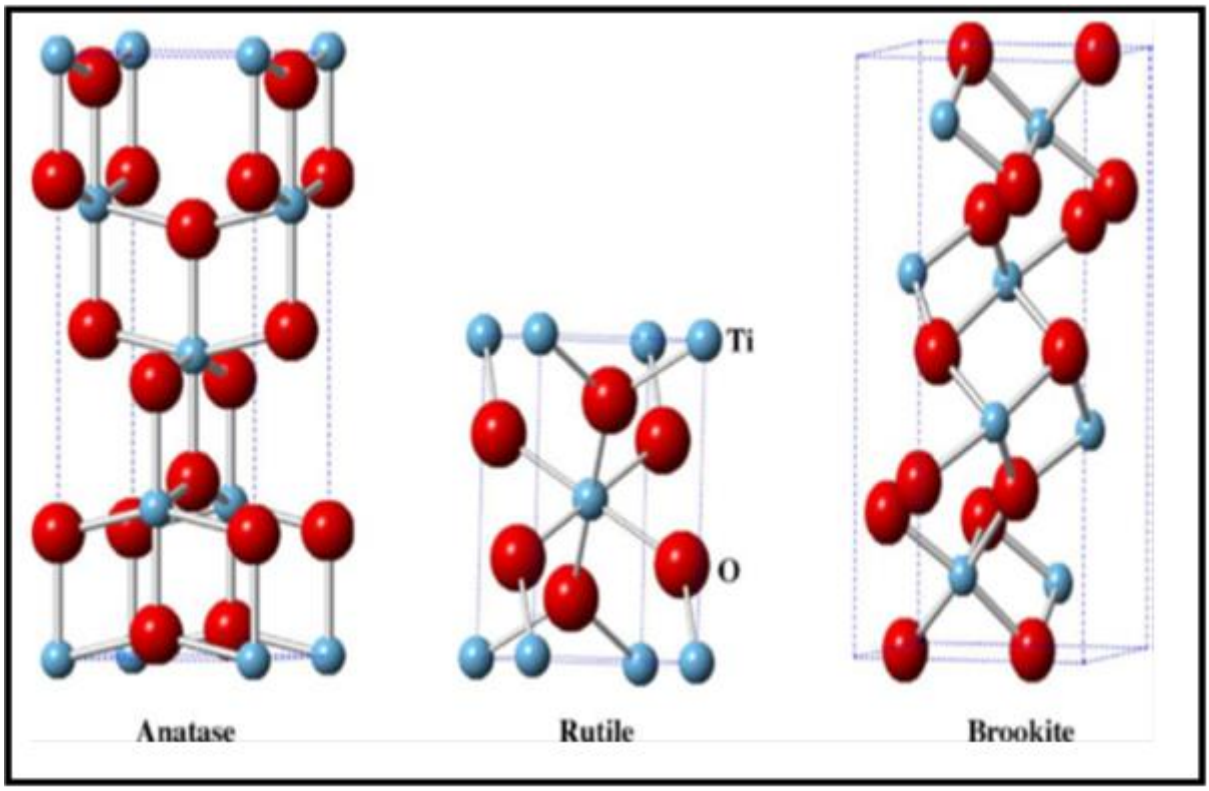


Figure I.11. Crystal structure of anatase, rutile and brookite [48].

I.3.1. Structural properties

Rutile phase

Rutile (tetragonal, space group $P4_1/mnm$) is made up of chains of TiO_6 octahedra connected by a vertex along the c-axis. Rutile has three primary crystal faces, two of which are low in energy and necessary for practical polycrystalline or powder materials. These faces are (110), (001), and (100), with the most thermally stable being (110). The rutile phase is stable at temperatures and pressures up to 60 kba, while the (001) face is thermally less stable. It is the most stable phase for particles larger than 35 nm in size [46].

Anatase phase

Anatase's (tetragonal, space group I41/amd) crystal structure is made up of distorted TiO_6 octahedral sites that share four corners. It also has two low-energy surfaces, (101) and (001), which are frequent in natural crystals. The (101) surface is the most common face for anatase nanocrystals. Anatase is the most stable phase for nanoparticles smaller than 11 nm, and its minimum fundamental band gap is indirect; it was determined experimentally to be 3.2 eV using electrochemical measurements at room temperature (RT). Anatase is the first phase to crystallise during heat treatment of amorphous TiO_2 [47].

Brookite phase

The brookite phase is rarer and more difficult to prepare. Brookite is the most stable phase for nanoparticles in the 11-35 nm range due to its orthorhombic space group Pbca structure with lower symmetry among counter-polymorphs. The octahedral sites are distorted and elongated along the c-axis, with each octahedron sharing three edges with adjacent octahedra. The order of stability of the crystal faces is 010 < 110 < 100 [46].

I.3.2. Stability of crystalline phases

The Gibbs free energy (G) of a nanoparticle system includes both the bulk free energy (Gb) and the surface free energy (Gs). Inequality in particular surface energies between polymorphs can cause a reversal in their Gibbs free energies at a specific size, affecting their relative phase stability. Gribb et al. [50] observed phase stability reversal in nanocrystalline TiO_2 as a function of particle size, which was supported by thermodynamic analysis and calorimetric determination by Zhang et al. [51] and Ranade et al. [52]. Smaller particles have larger surface/volume ratios, leading to higher free energy and stresses. For particle sizes below 14 nm, anatase polymorph is the most thermodynamically stable, followed by rutile for sizes above 35 nm and brookite for sizes between 14 and 35 nm [53, 54]. Anatase is the stable nanophase of TiO_2, while rutile is the stable bulk phase under high temperatures and pressures [55].

I.3.3. Optical properties

TiO_2 is characterized as a semiconductor with a broad bandgap. The band gaps of Rutile, Anatase, and Brookite are 3 eV, 3.2 eV, and 3.1 eV, respectively.

The gap (Eg) exists between the valence band, associated with the O 2p orbital, and the conduction band, linked to the Ti 3d orbital. These gap values result in transitions associated with photons in the ultraviolet spectrum. The transparency of TiO_2 in the visible spectrum, coupled with an absorption edge of about 0.42 µm, results in significant ultraviolet absorption, endowing it with remarkable qualities, including protection against UV radiation [56, 57].

The various forms of titanium oxide possess a high refractive index (n) in the visible spectrum. Rutile has the highest refractive index (n ~ 2.66) of the three stable crystalline phases. This is higher than the anatase type (n ~ 2.54). The combination of this property with

a diffusion coefficient for high visible light renders the Rutile phase a preferred white pigment for industrial applications, including paints, food, and pharmaceutical coloring [58, 59].

I.3.4. Electrical Properties

The bandgap of the n-type semiconductor TiO_2 is relatively large, in the range of 3.05-3.5 eV. The resistivity of single-crystal titanium dioxide (TiO_2) is given as 10^{13} Ω.cm at room temperature and 10^7 Ω.cm at 250°C. These values indicate a strong temperature dependence of the electrical properties.

The electrical conductivity of single-crystal rutile TiO_2 is 5 x 10^{-14} (Ω cm) $^{-1}$ at 30°C and 3.3 x 10^{-9} (Ω cm) $^{-1}$ at 260°C. Therefore, TiO_2 generally behaves as an insulator when the temperature is below 200°C.

Highly insulating TiO_2 films have numerous applications, including their use as ultra-thin gate dielectrics in MOSFET devices. However, the electrical characteristics of the TiO_2 film can be modified to make it highly conductive, which is used in applications such as corrosion-resistant electrodes and in gas and humidity sensors [60], as shown in Figure I.12.

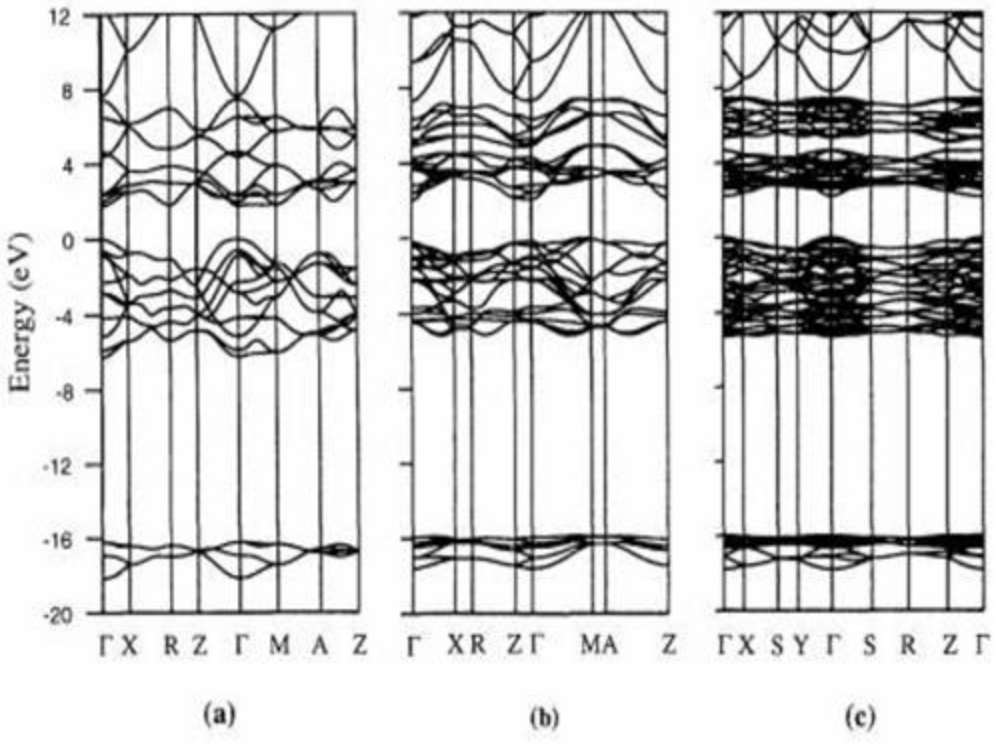


Figure I.12. TiO_2 band structure for rutile, anatase and brookite [49].

I.3.5. Titanium dioxide applications

✓ Photocatalyst

Photocatalysis is the enhancement of a photoreaction facilitated by a catalyst. The photocatalytic activity relies on the catalyst's capacity to generate electron-hole pairs that participate in secondary processes (equation I.5).

$$TiO_2 \xrightarrow{h\nu} TiO_2 + h^+_{BV} + e^-_{BC} \quad \text{(I.5)}$$

The identification of water electrolysis by TiO_2 rendered photocatalysis actually feasible. TiO_2 is the most prevalent semiconductor employed as a photocatalyst, characterized by its cost-effectiveness. It serves as an effective photocatalyst under ultraviolet light. When doped with nitrogen ions or metal oxides, it exhibits photocatalytic activity under visible light as well [61]. The anatase phase of TiO_2 is undoubtedly the most photochemically active [62]. The photocatalytic activity of TiO_2 arises from the production of OH radicals through the oxidation of OH^- anions (equation I.6) and the formation of O_2^- radicals via the reduction of O_2 (equation I.7).

$$OH^-_{ads} + h^+ \rightarrow OH^\circ_{ads} \quad \text{(I.6)}$$

$$O_2 + e^- \rightarrow O_2^{\circ -} \quad \text{(I.7)}$$

The schematic design in Figure I.13 illustrates that both radical anions can interact with other species, leading to their degradation or alteration, thereby establishing TiO_2 as an efficient photocatalyst for many applications. TiO_2 and ultraviolet radiation from the Sun can facilitate the decomposition of hydrocarbons in crude oil into water and carbon dioxide. The photocatalytic activity of TiO_2 is effective in eliminating oil slicks that float on the ocean's surface [22].

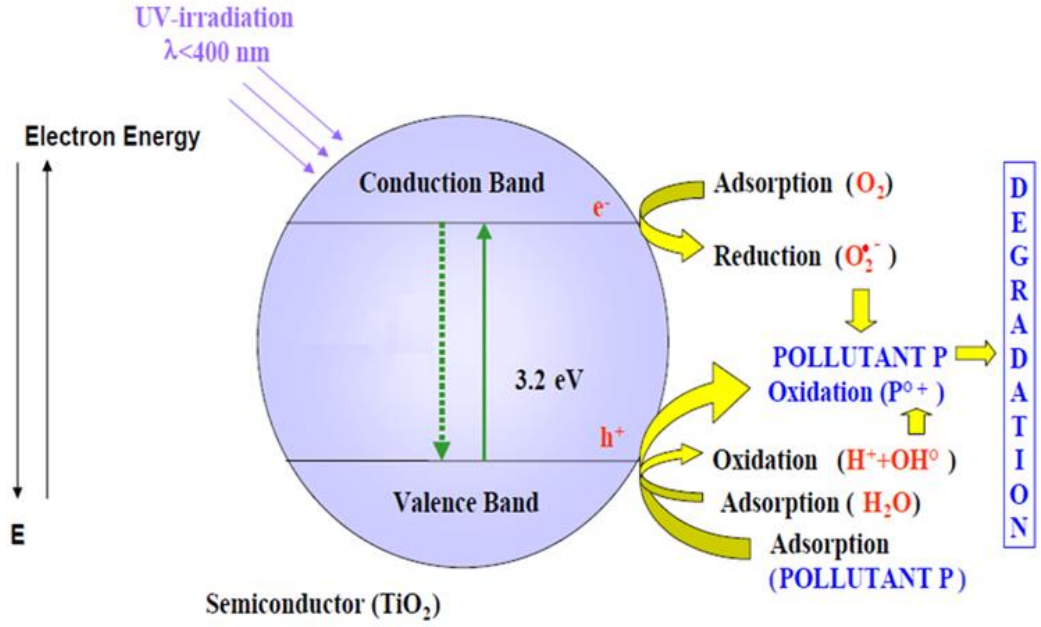


Figure I.13. General mechanism of photo-catalysis [63].

- ✓ **gas sensor**

The effect produced by the interaction between gas and solid, and, in particular, by the adsorption of molecules of gas (the adsorbate) on the surface of the film (the adsorbent), constitutes the basis of gas sensing. Oxidation and reduction reactions occur on the surface of the material following the gas-solid interaction, thereby leading to changes in one or more physical and chemical properties (mass, electrical conductivity, optical, etc.) of the sensor.

In some cases, in the presence of specific gases, the properties of the sensor become altered. In fact, the gas in question gets adsorbed either on the surface of the thin-film sensor or on the boundaries of the film. The molecule adsorbed may trap one of the electrons freely available. The phenomenon results in an electrical resistance increase. The ratio between the two resistivities before and after the gas exposure becomes known as sensor sensitivity. Adsorption of the gas under test on the surface of the sensor is not mandatory; it can interfere with the oxygen-containing species on the surface. The most commonly used substances as detectors are semiconductor oxides such as SnO_2, ZnO, WO_2, and TiO_2 [64, 65]. The importance of titanium dioxide for this topic should be emphasized due to its stability and good interaction with gases.

Typically, the construction of a gas detector includes a converter capable of converting the effect of the reaction between the gas and the sensitive element into an easily measurable

signal (electrical or optical) and the sensitive element itself, which is the key part of the sensor where the reaction with gaseous compounds occurs. It has been experimentally shown that the introduction of metals such as Pd, Pt, Au, Ru, Rh, and Ti into semiconducting oxides improves their sensitivity and selectivity [66], as well as accelerates the reaction with some gases. One possible way to evaluate the performance characteristics of TiO_2-based sensors is to synthesize heterostructured oxide nanomaterials [67].

✓ Solar cells

The conventional solar cells operate on the principle of a photovoltaic effect, occurring at the semiconductor junction. These solar cells share similarities with semiconductor devices such as integrated circuits and transistors in terms of fabrication techniques. The semiconductor absorbs light while simultaneously separating the created electric charges electrons and "holes." The electrons and holes are likely to recombine, so defects should be minimized in order for the process to occur effectively. Being rather expensive to manufacture, this type of cell cannot be utilized for mass power generation. A monolayer of dye, chemically adsorbed on the semiconductor's surface, ensures light absorption [68]. A dye with specific properties, typically a transition metal complex, will inject an electron into the semiconductor after excitation by a photon. The injected electron is then collected under the influence of the internal electric field. The redox mediator in the electrolyte accepts the positive charge from the dye and transfers it to the counter electrode. Thus, the final electron transfer completes the redox cycle and returns the mediator to its initial reduced state. The open-circuit voltage corresponds to the difference between the semiconductor Fermi level and the redox potential of the mediator [69].

I.3.6. Effect of annealing temperature

Annealing refers to the heating of materials at high temperatures to investigate their properties or improve them. These include phase transitions, recrystallization, polygonization, homogenization, internal stress relief, and removal of the effects of cold work. Such as strain hardening and defect removal. Kinetics of annealing, i.e, heating and cooling rates and time spent at a certain temperature, have a major effect on the outcome [70]. For this experiment, the temperature of annealing was changed from 300 to 500°C, while the difference between two successive readings was 100°C.

Chapter II

Elaboration technique and characterization tools

II.1. Preparation of the substrate

II.1.1. Choice of substrate

The studied films were deposited on glass substrates, with dimensions of 2.5cm× 2.5cm. The choice of glass as a deposition substrate was adopted for the following reasons:

1. Thermal compatibility with TiO_2 due to the close thermal expansion coefficients are α glass = 3.3 × 10^{-6} K^{-1} and α TiO_2 = 8−10 × (10^{-6} K^{-1}), which minimizes the stress at the film/substrate interface.
2. Their transparency, which is well suited for optical characterization of films in the visible region.
3. Low cost and wide availability.

II.1.2. Cleaning of the substrate

The substrates used for thin film preparation Figure II.1 must undergo a cleaning procedure, which is an important process before the start of the deposition technique. This process strongly affects the surface smoothness, uniformity, and porosity of the film.



FigureII.1. Photo of the glass substrate used.

The substrates are cut using a pen with a diamond point,

• Cleaning with a soap solution (2%),

• Rinsing with distilled water and then with acetone for 5 min.

• Rinsing with distilled water.

• Rinsing with methanol for 5 min at ambient temperature.

• Cleaning in a distilled water bath.

• Drying using hot air.

II.2.Preparation of the sol for TiO_2 thin film fabrication

All the reagents used in the synthesis of TiO_2 films are listed in the following TableII.1:

TableII.1.Different reagents used for the preparation of TiO_2 thin films by sol-gel

Product	Formula	Brand	Purity (%)
Titanium(IV) isopropoxide	$Ti(OCH(CH_3)_2)_4$	Aldrich	97+
Isopropanol	$CH_3CHOHCH_3$	Prolabo	99.8
Acetic acid	CH_3COOH	Prolabo	99.5
Methanol	CH_3OH	Prolabo	99

II.3.Deposition setup (dip-coating)

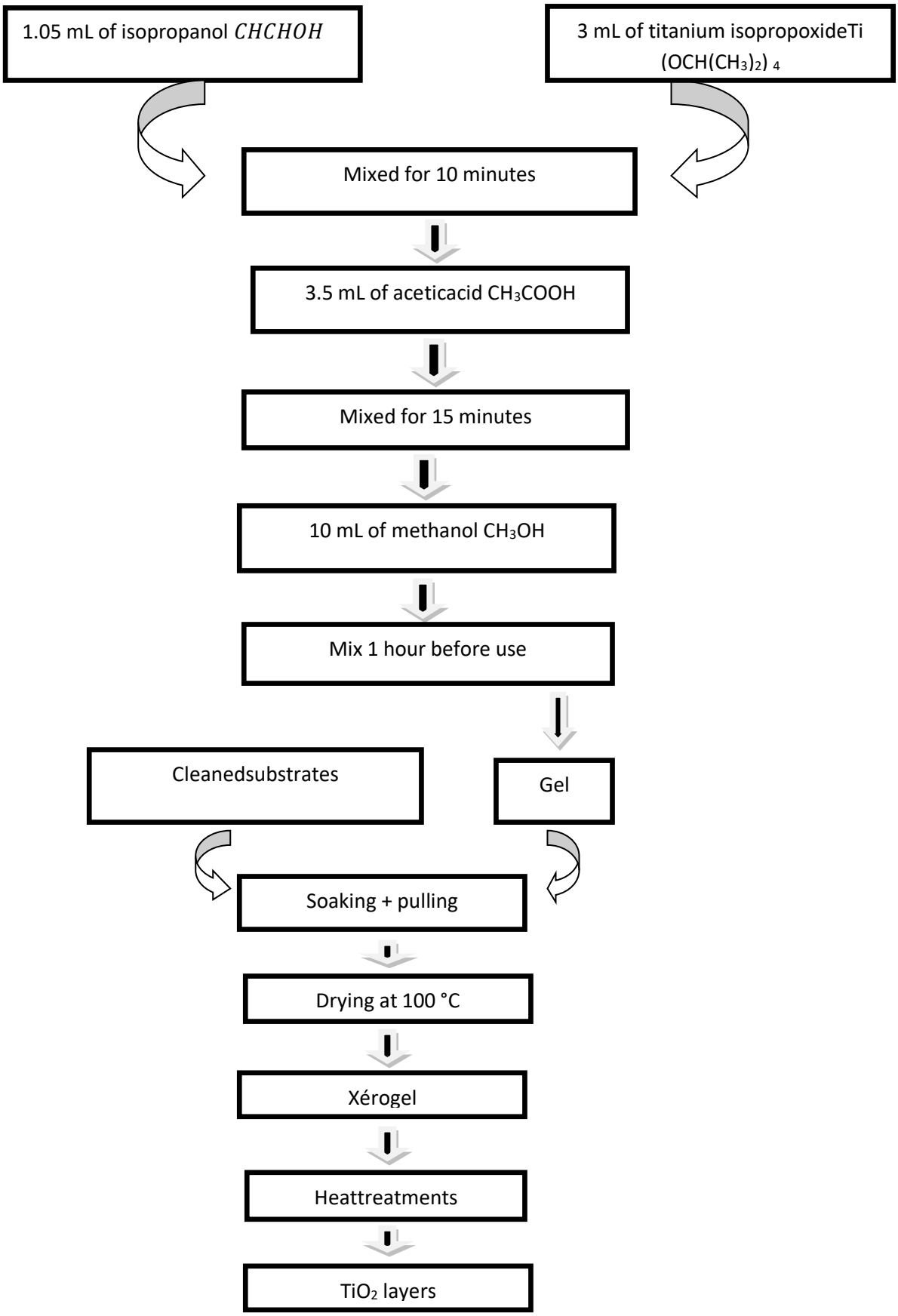
The deposition system (Model No.: HO-TH-02B) was used to deposit TiO_2 thin films onto flat substrates using the dip-coating technique. This work was carried out at the Thin Films and Interfaces Laboratory of the Frères Mentouri University—Constantine. A photograph of the dip-coating setup is shown FigureII.2.



Figure II.2.Experimental layer drawing device used at the Thin Films and Interfaces Laboratory of Constantine 1 University.

The substrate is first cleaned according to the standard procedure. After cleaning, it is carefully positioned above the solution contained in a vessel (beaker). The sample, attached to a rod by a clip, is then immersed into the solution at a constant speed selected via an appropriate setting. The substrate is kept immersed in the solution for several minutes (the immersion time varies from 1 to 10 minutes). Maintaining a stable liquid surface is essential to avoid the formation of striations on the sample. The substrate, now impregnated with the sol, is then withdrawn at a low pulling speed **(1200μm.s^{-1})** until it is completely removed from the solution. A multilayer deposition procedure (multiple dip-coatings) is adopted to obtain a final three layer TiO_2 coating (3 layers of TiO_2).

After the deposition of each (mono) layer, the sample is dried at 100°C for 10 minutes. The final prepared deposit is heat-treated for 1 hour at 500°C.The experimental procedure is summarized in the following schematic diagram Figure II.3



FigureII.3.Schematic flowchart for the preparation of TiO_2 thin films.

II.4.The annealing or heat treatment

Annealing process is considered the final stage in the preparation of thin films, where the samples are annealed at 500 °C for one hour in a furnace. This process removes the residual organic species present in the initial solution and promotes material densification and crystallization of the material. Figure II.4 shows photographs of the prepared samples.

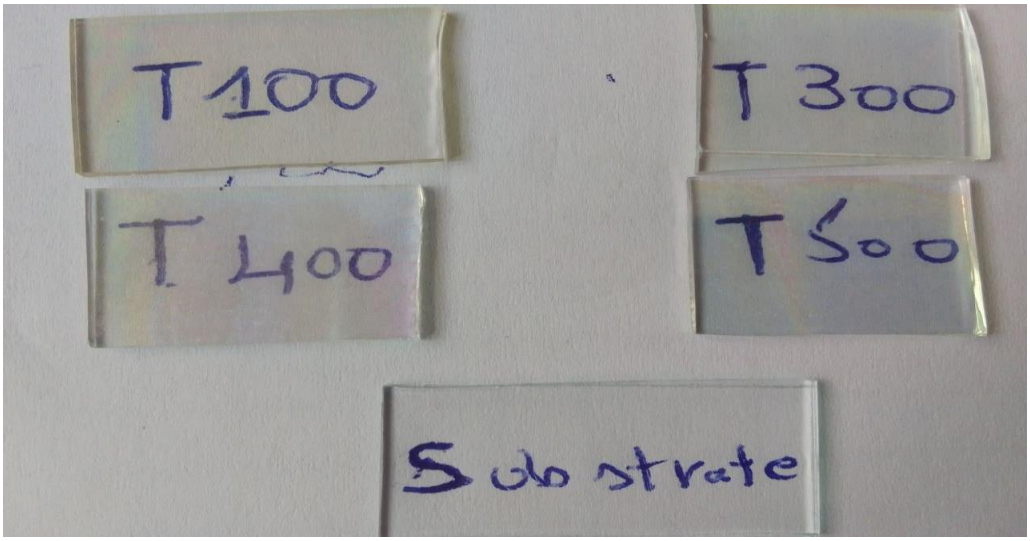


Figure II.4. A photograph of the TiO_2 samples as a function of the annealing temperature for TiO_2 films.

II. 5.Characterization techniques of thin films

II. 5.1. Structural characterization with X-ray diffraction

X-rays are electromagnetic waves with a short wavelength. X-rays occupy the electromagnetic spectrum region between gamma rays and ultraviolet radiation [71].

$$E = \frac{hc}{\lambda} \qquad (II.\ 1)$$

Due to their short wavelength (λ), X-rays possess relatively high energy. The entire field of crystallography is based on a simple relation established by W.L. Bragg in 1912, which describes the condition for X-ray diffraction. This relation, known as Bragg's Law is expressed as follows [72]:

$$2d_{hkl}\sin\theta = n\lambda \qquad (II.\ 2)$$

With d_{hkl} being the interplanar spacing. The interplanar diffraction angle is given as θ and the wavelength of the X-ray, as illustrated in FigureII.5.

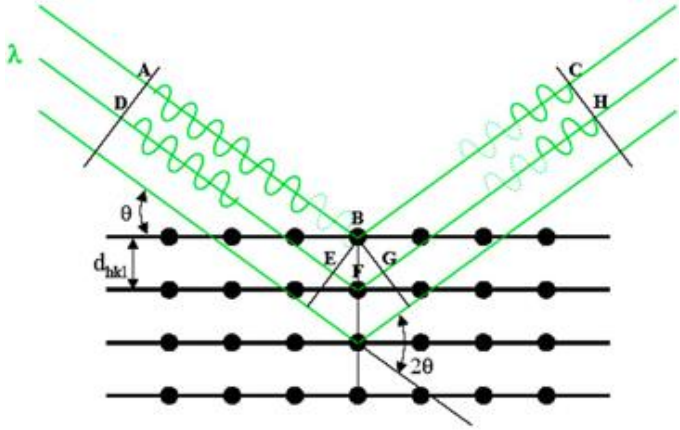


Figure II.5. Principle of XRD [74].

X-rays are extremely useful for studying the atomic arrangement of crystalline materials due to their short wavelength and high energy levels. As illustrated in Figure II. 6, Bragg's Law can be used to calculate the distance and thus determine the crystal structure of the material.

It should be noted that the shape of the diffraction peaks is closely related to the crystal structure of the sample. By analyzing the location of the diffraction peaks as well as the intensity of the diffracted peaks, various properties of the sample can be determined [73].

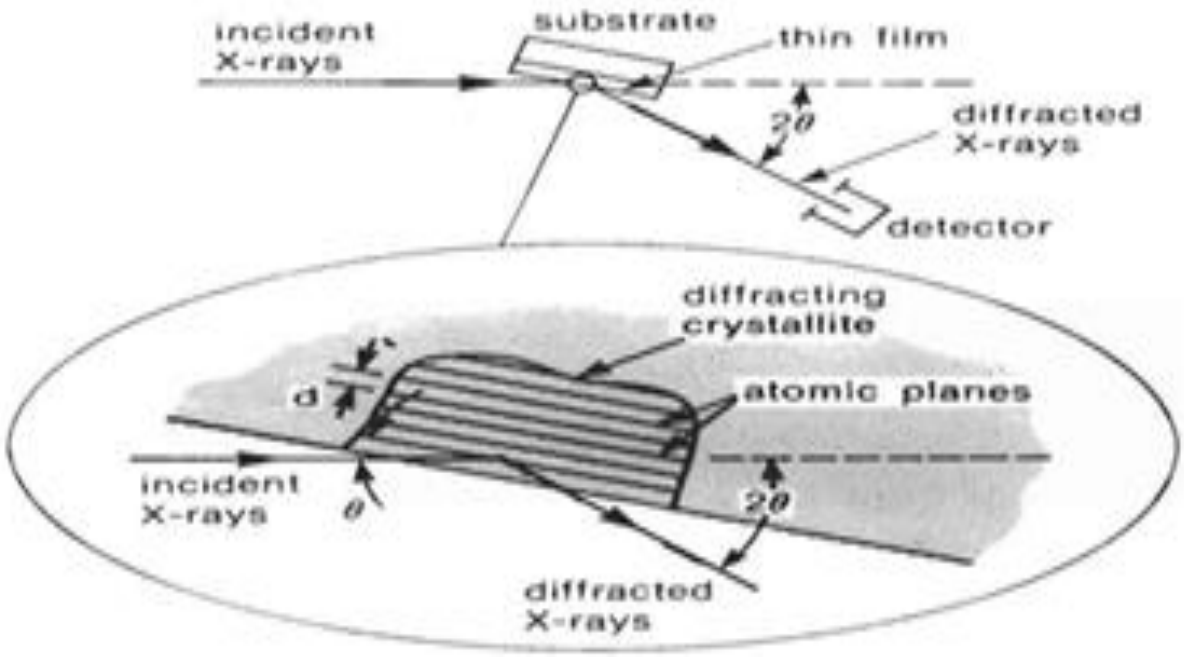


Figure II.6. Basic features of a typical XRD experiment [74].

Thin films prepared TiO_2 were checked by X-ray diffractometer using Cukα radiation of wavelength λ = 1.5418 Å from Bruker AXS.D8 diffractometer to examine the crystal structure

II. 5.1.1.Determination of crystallite size

The crystallite size can be determined from the FWHM of the highest intensity diffraction peak using the Scherrer equation [75].

$$D = \frac{0.9\lambda}{\beta\cos\theta} \quad \text{(II.3)}$$

D represents the average crystallite size, the wavelength of the X-ray is denoted by λ, the full width at half maximum for the peaks is represented by β, and θ is the Bragg angle [76]. As illustrated in Figure II.7, the parameter β is defined from the X-ray diffraction peak profile.

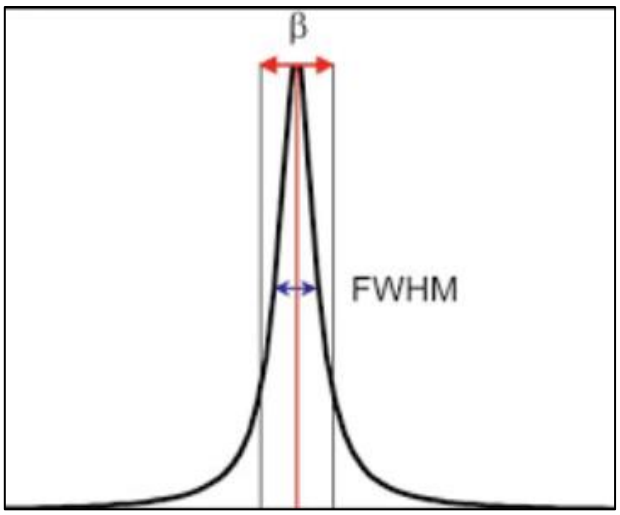


Figure II.7. Definition of β from the diffraction curves [76]

II. 5.1.2.Determination of the lattice parameters

The lattice parameters (a=b, c) have been found using the following equation [77]:

$$\frac{1}{d^2} = \frac{(h^2+k^2)}{a^2} + \frac{l^2}{c^2} \quad \text{(II.4)}$$

a and c: the lattice parameters; h, k, l: the Miller indices of the planes; d_{hkl}: the interplanar spacing. These values of a, b, and c can be obtained from this equation and later compared with the data. Theoretically determined values, which are available in the ASTM database [78].

II.5.2.Atomic Force Microscopy (AFM)

Atomic Force Microscopy is a type of Scanning Probe Microscopy (SPM).This technique uses a sharp probe tip that measures the interaction forces over the sample surface. AFM is used to investigate the surface morphology of samples using a sharp probe tip.

Therefore, it becomes possible to determine grain size and obtain data on surface roughness [79].

The principle of the atomic force microscope involves the use of an extremely sharp tip, which is mounted on a flexible cantilever. The interaction force between the scanning tip and the sample surface is measured. A laser diode is used to measure the deflection of the cantilever. Light emitted from the diode is focused on the back of the cantilever and then is reflected toward the photodetector. As a result of this, the reflected beam is displaced due to the deflection of the cantilever [80]. Figure II.8 illustrates the schematic configuration and working principle of the Atomic Force Microscope (AFM).

Atomic Force Microscopy has several operating modes. Surface topography can be generated through classical techniques such as contact mode, non-contact mode, and tapping mode, whereas other modes, such as MFM mode, EFM, and LFM, among others, provide additional information regarding the physicochemical properties of the sample [81].

Surface morphology analysis was carried out using a Flex-Axiom Nanosurf Atomic Force Microscope (AFM) with a C3000 controller.

The surface roughness of the thin films was evaluated using AFM. The root mean square (RMS) roughness is commonly used to evaluate surface roughness [60].

$$\mathrm{RMS} = \sqrt{\frac{\sum_{n=1}^{N}(Z_n - \bar{Z})^2}{N}} \qquad \text{(II.5)}$$

Where Z_n is the height of the nth data point, $\bar{z}$ is the mean height, and N is the total number of measured points.

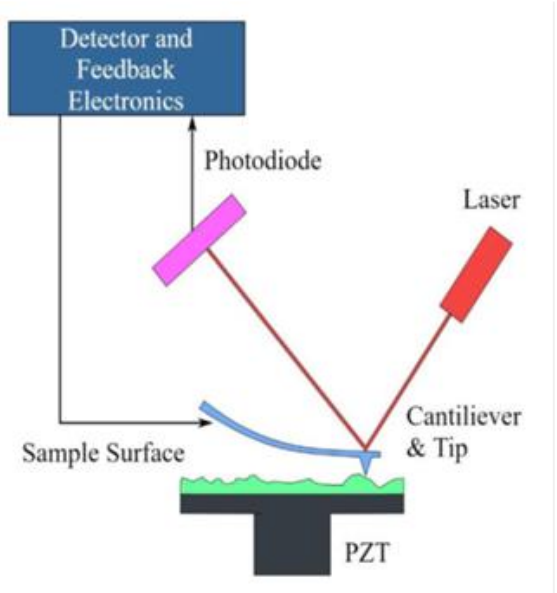


Figure II. 8. Schematic diagram of Atomic Force Microscope (AFM) [79].

II.5.3.Optical characterization and measurement

II.5.3.1. Ultraviolet-visible spectroscopy

The UV-visible spectrophotometer operates on the principle of analyzing the interaction of photons matter in the ultraviolet (200-400 nm) and visible (400-800 nm) regions. This absorption spectroscopy technique is based on the excitation of electrons from the ground state to higher energy levels. A schematic representation of the UV-Visible spectrophotometer is shown in Figure II.9.

Fluorescence results from the transition of electrons from an excited state back to the ground state. The Beer-Lambert Law is widely used for quantifying absorbing entities [39].

$$I = I_0 e^{(-\alpha d)} \quad \text{(II.6)}$$

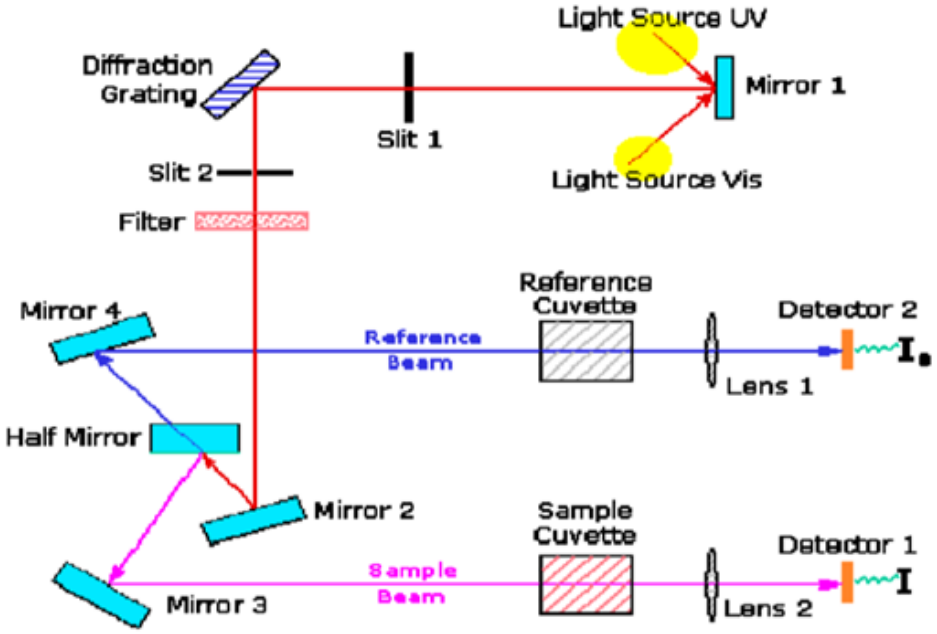
Where α is the absorption coefficient, d is the thickness of the film, I_0 and I represent the intensities of the incident and transmitted beams, respectively. The absorption coefficient (α) can be computed with the following formula:

$$\alpha = \frac{1}{d} \ln \left(\frac{100}{T(\%)} \right) \quad \text{(II.7)}$$

Where T (%) is the transmittance (quantity of the transmitted light), and can be directly measured by

$$T(\%) = \frac{I}{I_0} \times 100 \quad \text{(II.8)}$$

UV-Vis spectroscopy is based on the principle that when a monochromatic light beam passes through an absorbing medium, its intensity decreases with increasing thickness. The absorption of light is directly proportional to both the optical path length and the concentration of the absorbing species, according to the Beer–Lambert law [39].



FigureII.9.Schematic representation of UV-Visible Spectrophotometer [82].

In our experiment, we used a JASCO V-730 UV-Visible spectrophotometer.

II. 5.3.2.Determination of thin film thickness (d)

The thickness of the thin film was determined using the following equation:

$$d = \frac{\lambda_1 \lambda_2}{2(\lambda_1 n_2 - \lambda_2 n_1)} \qquad \text{(II.9)}$$

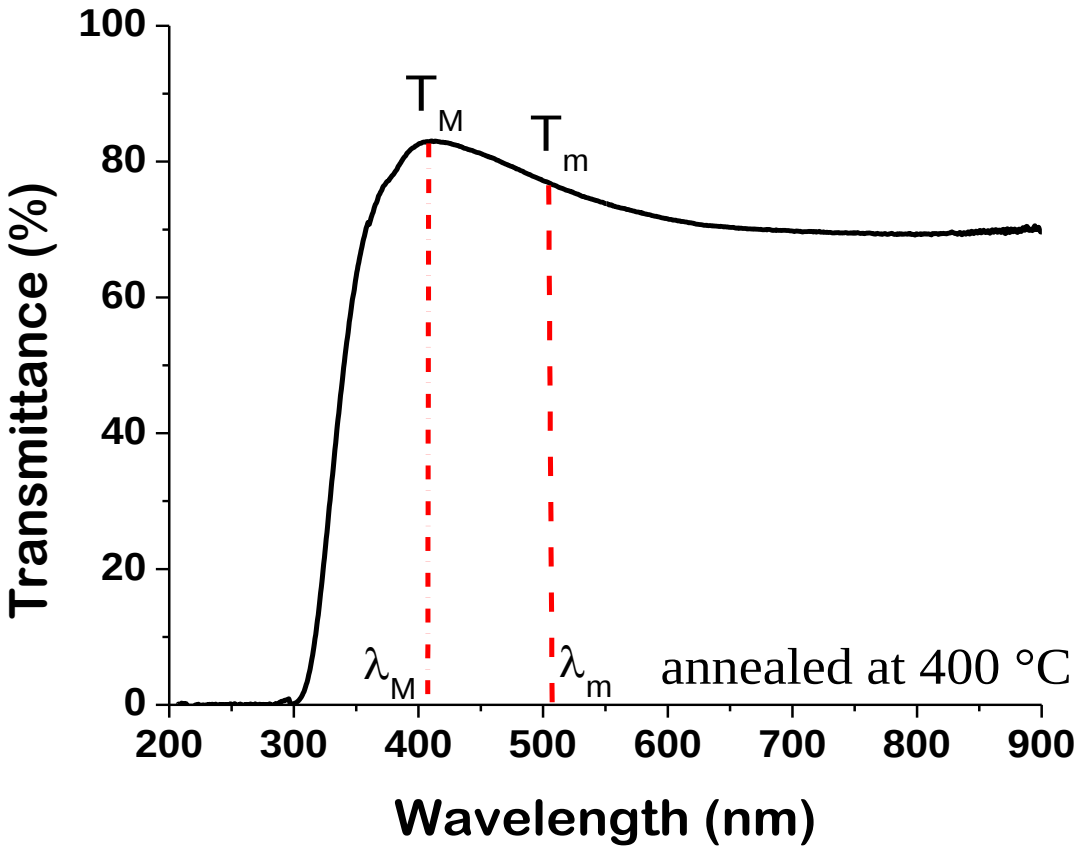
Where n_1 and n_2 are the refractive indices of the film corresponding to the wavelengthsλ_1 and λ_2 respectively, the refractive indices n_1 and n_2 can be calculated using the following relation:

$$n_{1,2} = [N_{1,2} + (N_{1,2}^2 - S^2)^{1/2}]^{1/2} \qquad \text{(II.10)}$$

Where S is the refractive index of the substrate, $N_{1,2}$ can be calculated using the following relation:

$$N_{1,2} = 2S\left[\frac{T_M - T_m}{T_M * T_m}\right] + \left(\frac{S^2+1}{2}\right) \qquad \text{(II.11)}$$

T_M: maximum transmission; T_m is the minimum transmittance located between two adjacent maxima.



FigureII.10. Interference fringes used for film thickness determination.

II.5.3.3.Determination of the absorption coefficient (α)

The Beer-Lambert law can be used to determine the absorption coefficient and extinction coefficient (k) of a thin film from its transmission spectrum [83].

$$T = e^{-\alpha d} \qquad \text{(II.12)}$$

The absorption and extinction coefficients are given by:

$$\alpha = \frac{1}{d} \ln\left(\frac{100}{T(\%)}\right) \qquad \text{(II.13)}$$

Where d is the film thickness and T is the transmittance.

II.5.3.4.Determination of the optical band gap (Eg)

To determine the optical band gap of a thin film in the high-absorption region, the Tauc relation is used [83].

$$(\alpha\, h\, \nu)^n = A(h\nu - E_g) \qquad \text{(II. 14)}$$

Where (hν) is the photon energy, Eg the optical band gap energy, and A is a constant. For n = 1/2, the experimental data exhibit the best linear behavior in the band-edge area,

indicating a direct allowed transition. The optical band gap is determined by plotting $(\alpha h\nu)^{1/2}$ versus photon energy ($h\nu$) and extrapolating the linear portion to the energy axis. Band- tails states appear near the band edges due to localized states at the edge. These band-tail states are responsible for absorption in the low energy range. In this range, the absorption coefficient is expressed as

$$\alpha (h\nu) = \alpha_{o} \exp (h\nu/E_U) \qquad \text{(II.15)}$$

In this equation, α_0 represents the pre-exponential factor, hv is photon energy, and E_U is the band tail width or energy of disorder, also known as the Urbach tail. E_U can be estimated from the inverse slope of the linear region. The linear figure shows the relationship between ln (α) and hv [84].

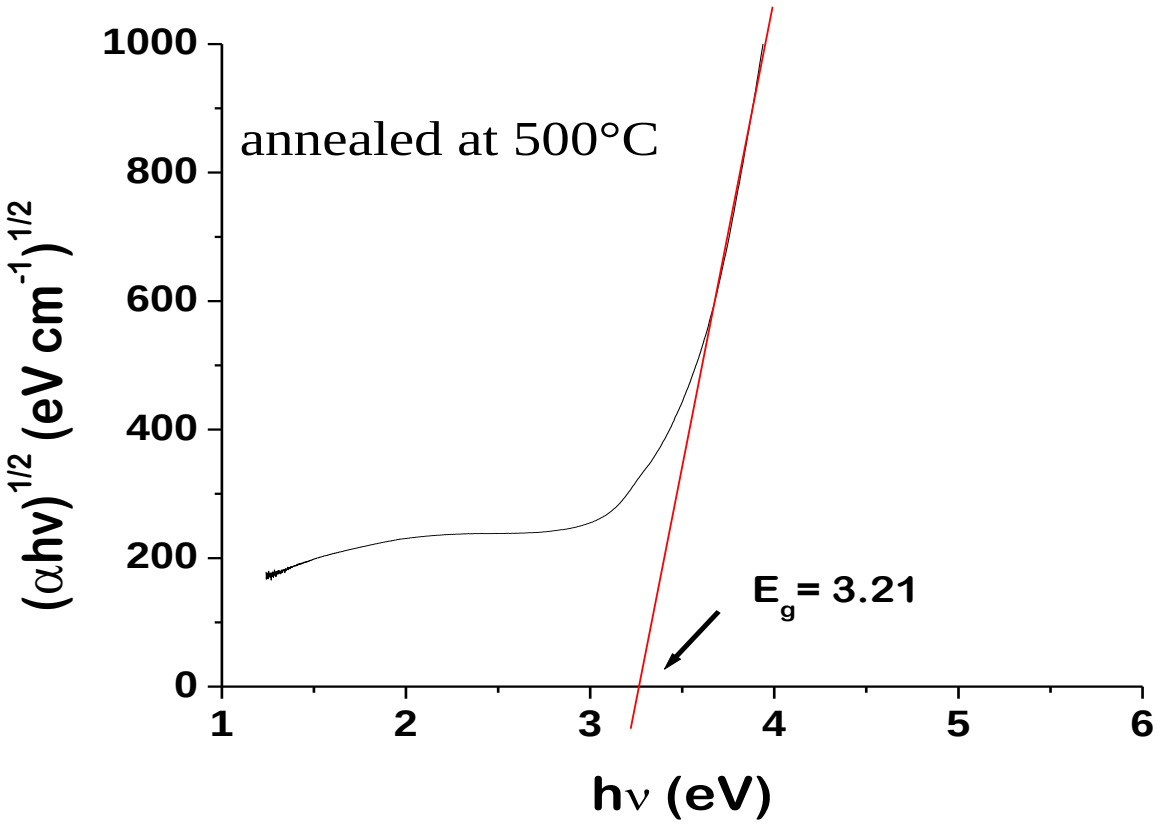


Figure II.11.Determination of optical band gap

II.5.3.5. Urbach energy (E_u)

Urbach energy (E_u) indicates the degree of structural disorderin a film. For semiconductors, fundamental absorption shows an exponential increase as the photon energy approaches the band-gap energy. The Urbach energy (the width of the exponential absorption tail) can be determined from [82].

$$\alpha = \alpha_0 \exp\left(\frac{h\vartheta}{Eu}\right) \quad \text{(II.16)}$$

Where α_0 is a Constant and E is the Urbach Energy.

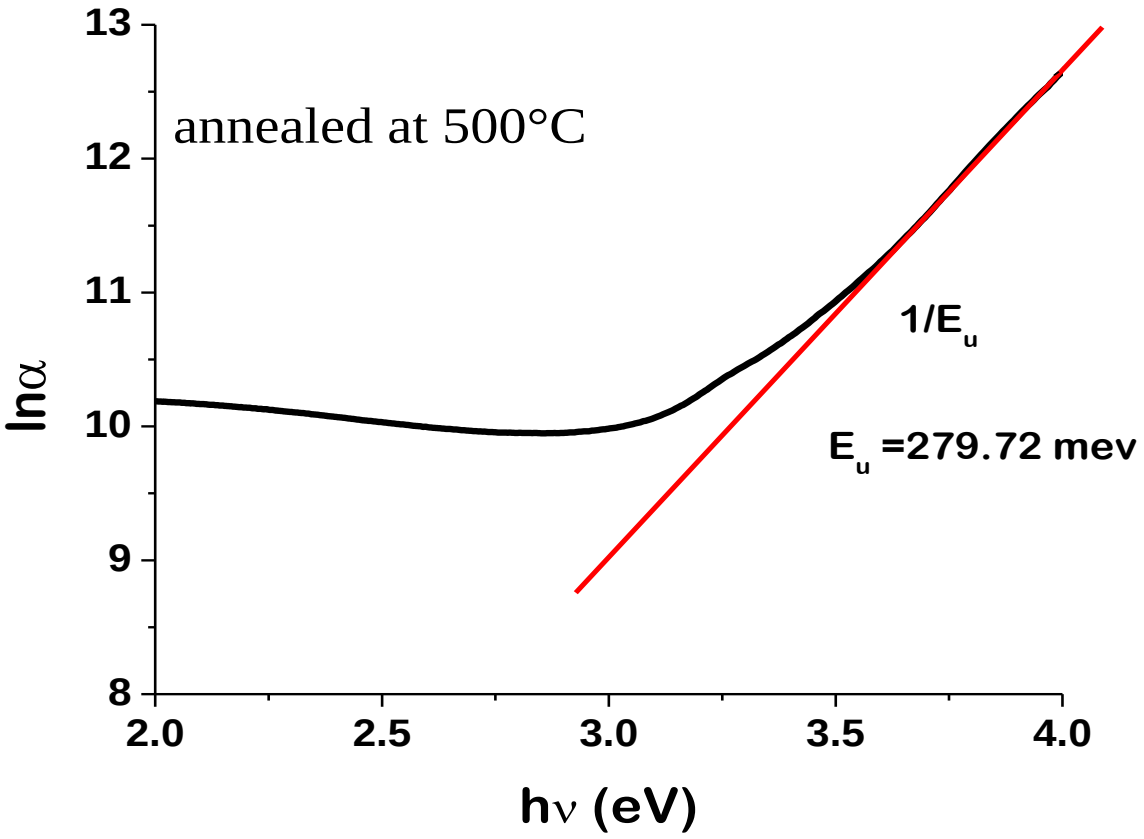


Figure II.12. Determination of Urbach energy

Chapter III

Experimental results and discussion

III.1. Structural Studies

III.1.1. XRD analysis

Figure III.1 (a) displays the X-ray diffraction (XRD) patterns of the as-deposited TiO_2 films, clearly demonstrating their amorphous nature before thermal treatment. Following annealing at 500°C for one hour, the XRD pattern exhibits a distinct peak at 2Θ = 25.5°, which corresponds to the (101) crystallographic plane of the anatase phase as shown in Figure III.1 (b). This emergence indicates a partial structural transition from an amorphous state to a polycrystalline anatase phase.

This behavior confirms the crystallization of TiO_2 films after thermal treatment and is in agreement with the findings reported by He et al. [85]. Furthermore, the crystallite size of the TiO_2 films was evaluated from the line broadening of the (101) reflection peak using the Scherrer equation [86].

$$D_{(nm)} = \frac{0.9\lambda}{\beta\cos\theta} \qquad \text{(III.1)}$$

Where D represents the crystallite size, λ is the wavelength of X-ray (λ CuKα= 1.5406 Å), β the peak full-width at half-maximum and θ the diffraction angle. The crystallite size of TiO_2 films was estimated to be approximately 11.5 nm, in good agreement with the results reported in literature [87, 88].

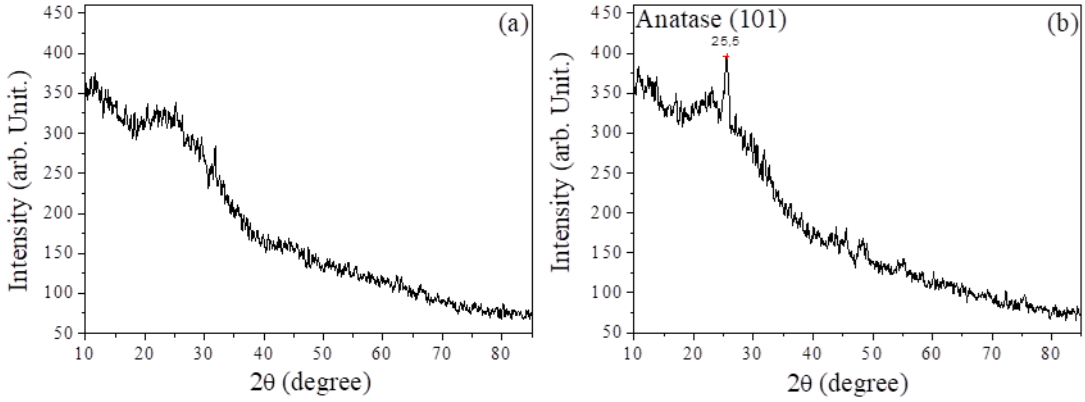


Figure III.1. X-ray diffraction patterns of thin TiO_2 films on glass substrates.

III.2. Surface morphology analysis by AFM

The surface morphology and roughness of the deposited TiO_2 films as a function of annealing temperature were analyzed using atomic force microscopy (AFM).

The roughness evolution was investigated over a scan area of 3 µm, as illustrated in Figure III.2 (a) - (d). The as-deposited TiO_2 film exhibits no significant crystalline formation, as shown in Figure III.2 (a), except for a limited number of nanocrystallites with diameters ranging from 10 to 20 nm, discontinuously distributed across the surfaces. Increasing the annealing temperature enhances the growth of the TiO_2 crystalline grains. At 300°C, crystalline grains of varying shapes and sizes begin to develop on the film surface. Their non-uniformity is attributed to insufficient thermal energy for homogenization.

Upon further annealing between 400°C and 500°C, the density of crystalline grains increases significantly, eventually covering nearly the entire film surface. The sample annealed at 500°C exhibits finely divided and monodispersed TiO_2 nanocrystalline grains, indicating improved crystallinity and grain growth.

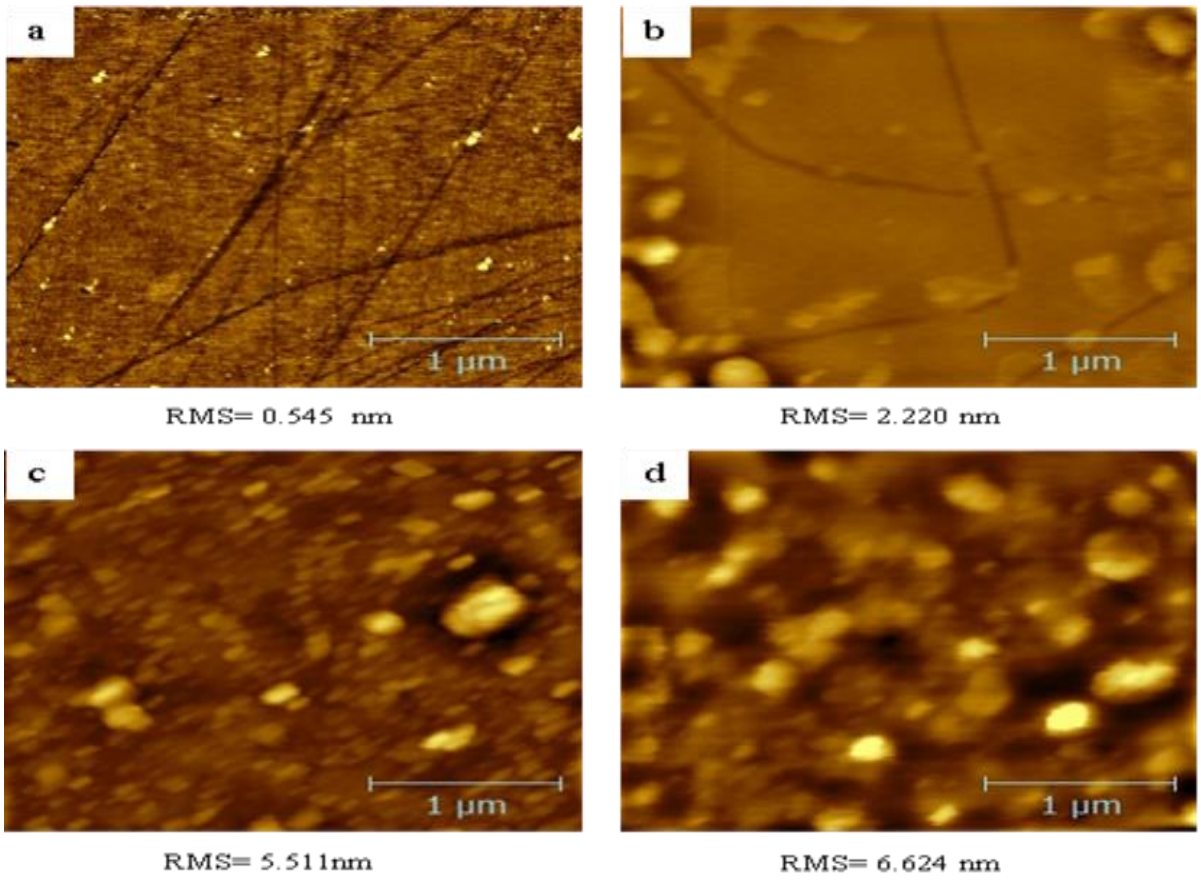


Figure III.2. 2D AFM images of TiO2 films

In addition to the presence of a high density of nanometric grains, the annealed samples exhibit increased surface roughness. The roughness was quantified using the root mean square roughness (Rms) parameter shown in Figure III.3. The RMS roughness increases significantly with increasing annealing temperature.

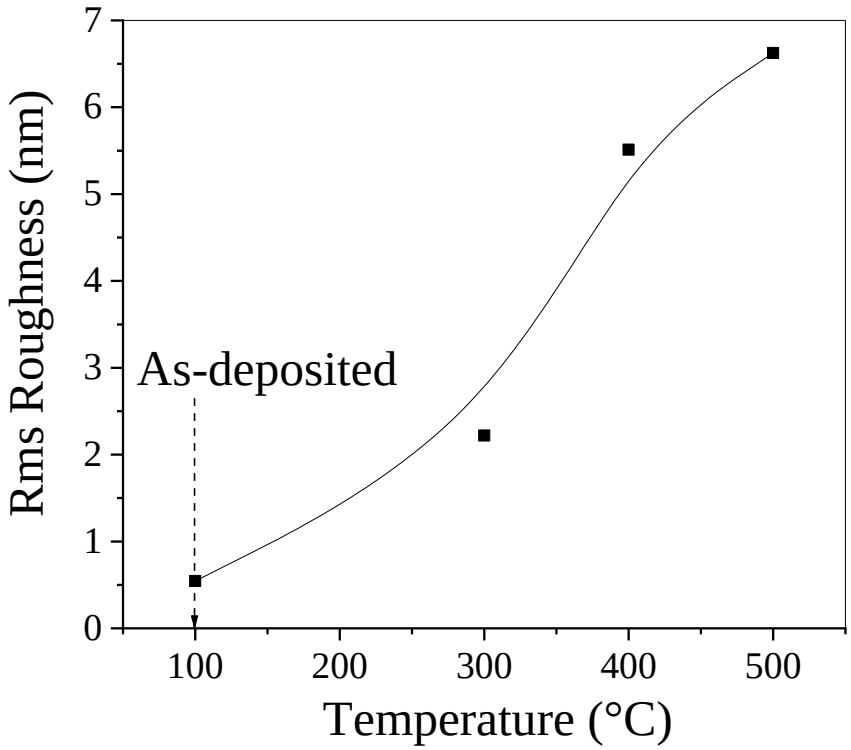


Figure III.3.RMS roughness of TiO_2 thin films as a function of annealing temperature.

While the root-mean-square (RMS) roughness shown in Figure III.3 exhibits only a slight variation between the as-deposited and the 300°C annealed samples, a significant increase is observed for the sample annealed at 400°C. The roughness shows only a slight variation for the sample annealed at 500°C. This behavior is attributed to the gradual crystallization of the material into the anatase phase, accompanied by the relaxation of elastic stresses accumulated during film growth [89]. These observations are in good agreement with the XRD results.

Consequently, the optical characteristics of the TiO_2 films, such as transmittance, refractive index, and birefringence, are expected to be influenced by the surface morphology and roughness.

III.3. Optical properties

III.3.1. UV–vis analysis

Figure III.4 illustrates the transmission spectra of the TiO_2 films subjected to different annealing temperatures. The films exhibit high transparency in the visible region, while the onset of absorption occurs in the 310–370 nm range. The interference fringes observed in the 400–800 nm spectral range for the as-deposited film are attributed to its higher optical thickness.

In contrast, the absence of these oscillations in the annealed samples indicates a significant reduction in film thickness. Moreover, as the annealing temperature increases, the absorption edge shifts toward lower energies, indicating a reduction in the optical band gap energy of the films due to improved crystallinity and reduction of structural defects. This quantitative shift in the absorption edge, as derived from the transmission data shown in Figure III.4, demonstrates excellent agreement with the band gap energy trends presented in Figure III.6.

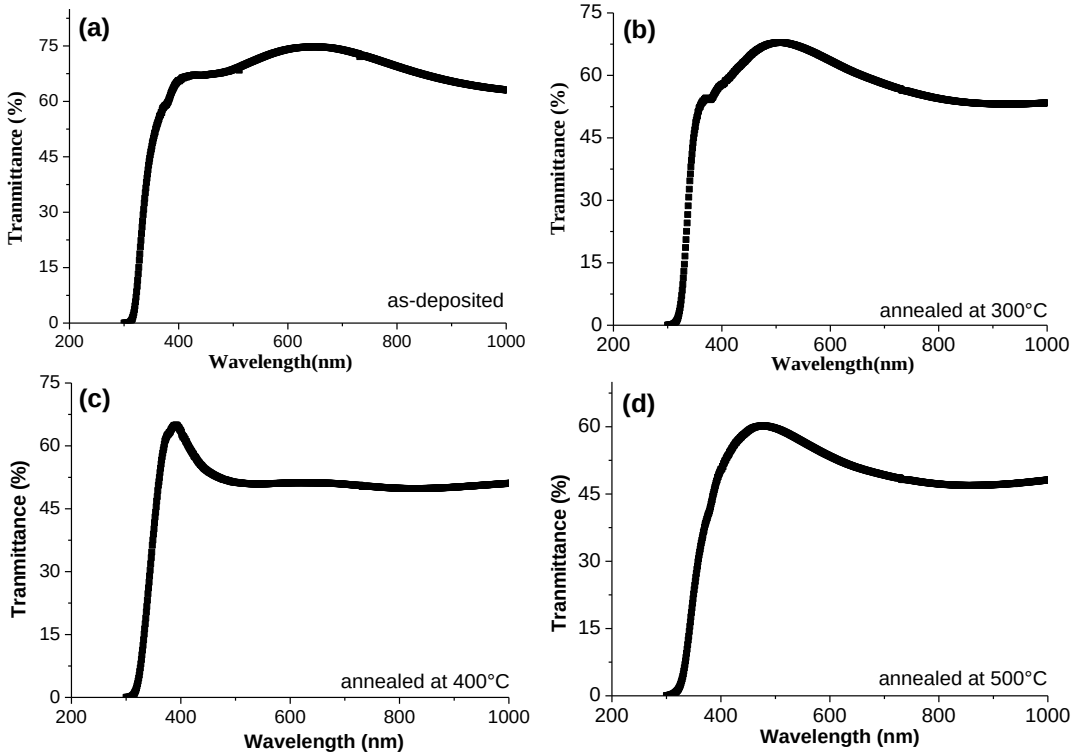


Figure III.4. UV–vis transmittance spectra of TiO_2 films.

Furthermore, Figure III.5 (a) demonstrates a decrease in the transmittance of the TiO_2 films with increasing annealing temperature, indicating higher absorption in films annealed at elevated temperatures.

This behavior can be attributed to enhanced surface scattering, which arises from increased surface roughness associated with higher film crystallinity. To further support this interpretation, the dependence of the average transmittance T_{av} in the visible region (around 633 nm) was determined as a function of the annealing temperature (Figure III.5) and correlated with the surface roughness values derived from the AFM measurements (Figure III.3). The results, presented in Figure III.5 (b), exhibit an excellent correlation between these two independent datasets, thereby confirming the influence of surface roughness on optical transmission.

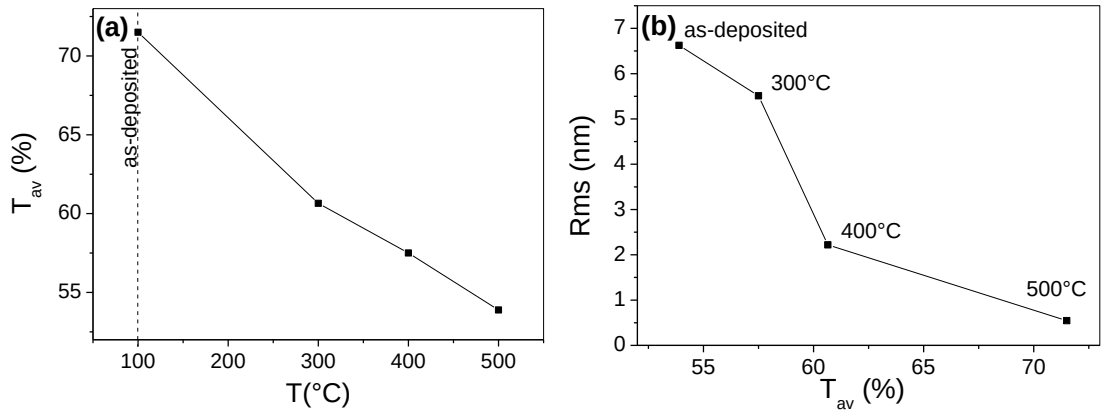


Figure III.5. (a) Average optical transmission at 633 nm vs annealing temperature. (b) Correlation between surface roughness and visible transmittance vs annealing temperature.

III.3.1.Band gap and Urbach energy

a) Band gap

Another valuable insight that can be extracted from the evolution of the transmittance spectra in Figure III.5 (a) is the optical band gap E_g of the TiO_2 films. To determine this parameter, the Tauc model was applied under the assumption of a predominant indirect allowed transition mode [90, 91], which is expressed as follows:

$$A \times (h\nu - E_g) = (\alpha h\nu)^{1/2} \quad \text{(III.2)}$$

Where A is the Const, hν is the photon energy, α is the absorption coefficient, d is the thickness determined from the optical interference analysis described in chapter II.

Figure III.6 (a) summarizes the plots of $(\alpha h\nu)^{1/2}$ versus photon energy (hν), showing a good linear dependence according to equation (III.2). Analysis of these results indicates that the optical band gap decreases with increasing annealing temperature, as clearly illustrated in Figure III.6, which depicts the variation of the extrapolated band gap energies of the TiO_2 films as a function of annealing temperature.

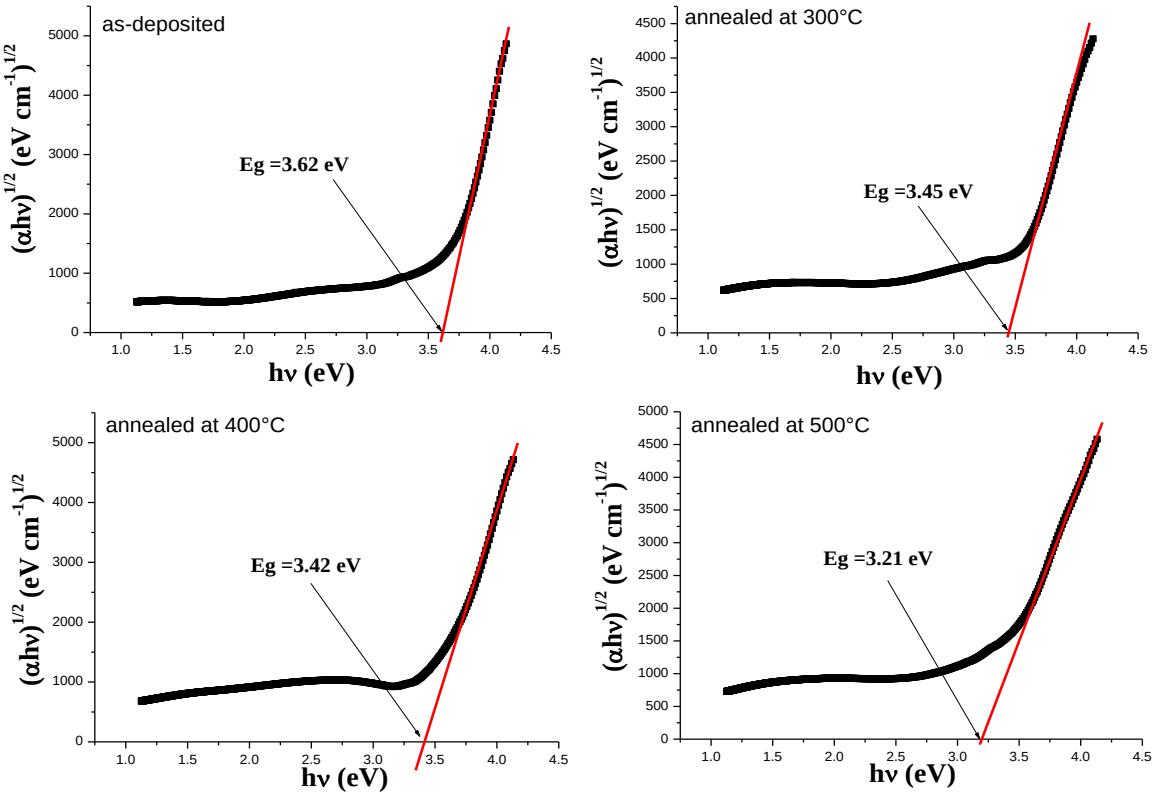


Figure III.6. Optical absorption spectra $(\alpha h\nu)^{1/2}$ versus energy (hν).

The as-deposited films exhibit a high optical band gap of E_g = 3.62 eV. Thermal annealing at 300–400°C leads to decrease in this value to E_g = 3. 42eV.

However, upon annealing at 500°C, the crystalline structure of the TiO_2 films in the anatase phase is substantially improved, and E_g decreases noticeably to 3.21 eV, which is reasonably consistent with the reported anatase TiO_2 band gap value of approximately 3.20 eV. Consistently, previous investigations have also reported a decrease in the band gap energy as film crystallinity increases [92, 93].

Furthermore, the optical band gaps of all synthesized TiO_2 thin films remain greater than that of bulk anatase TiO_2 (~ 3.2 eV). This increase may be attributed to quantum confinement effects within the thin films, as well as the thermal stress induced by the mismatch in thermal expansion coefficients between the fused glass substrate and the TiO_2 films [94].

b) Urbach energy

To evaluate the structural disorder through the Urbach energy (E_u) of the TiO_2 thin films, the logarithm of α was plotted as a function of hν (See Equations II.18) in order to obtain the value of E_u.

Figure III.7 presents the determination of disorder by extrapolation from the variation of ln α as a function of hν, for thin layers of TiO_2 as a function of the annealing temperature: a) as-deposited; b) 300°C; c) 400°C; d) 500°C.

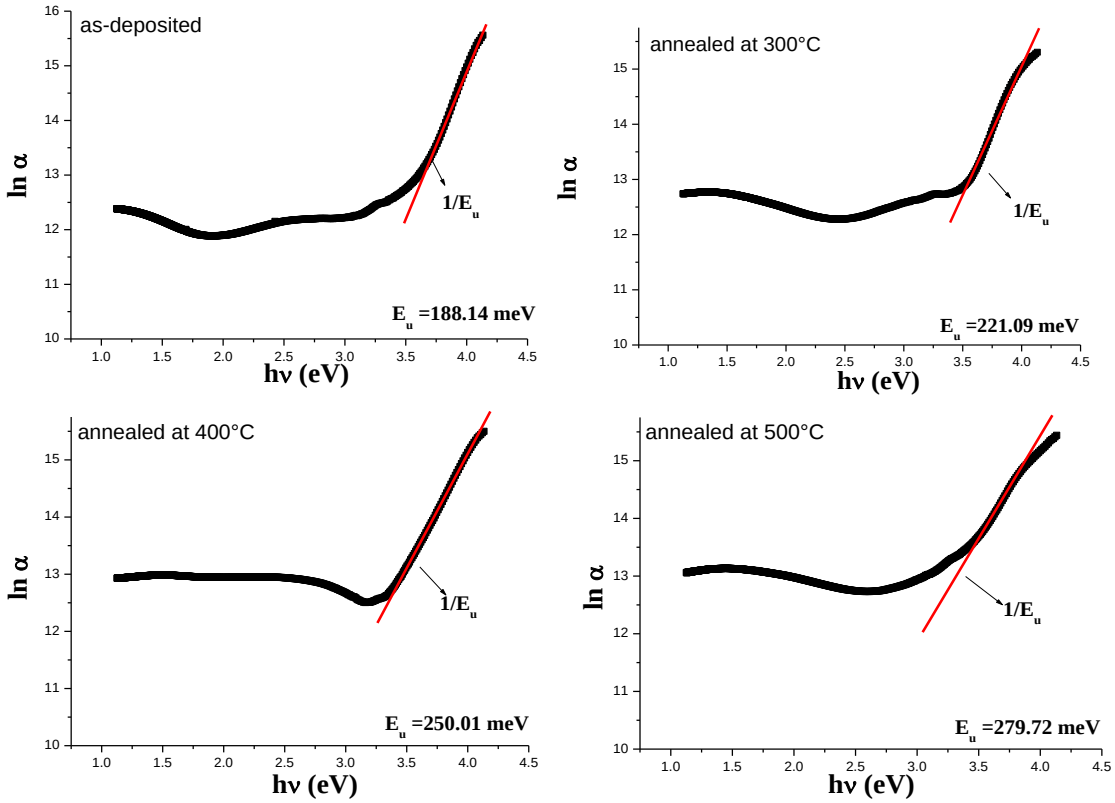


Figure III.7 variation of ln (α) as a function of hν in TiO2 thin films.

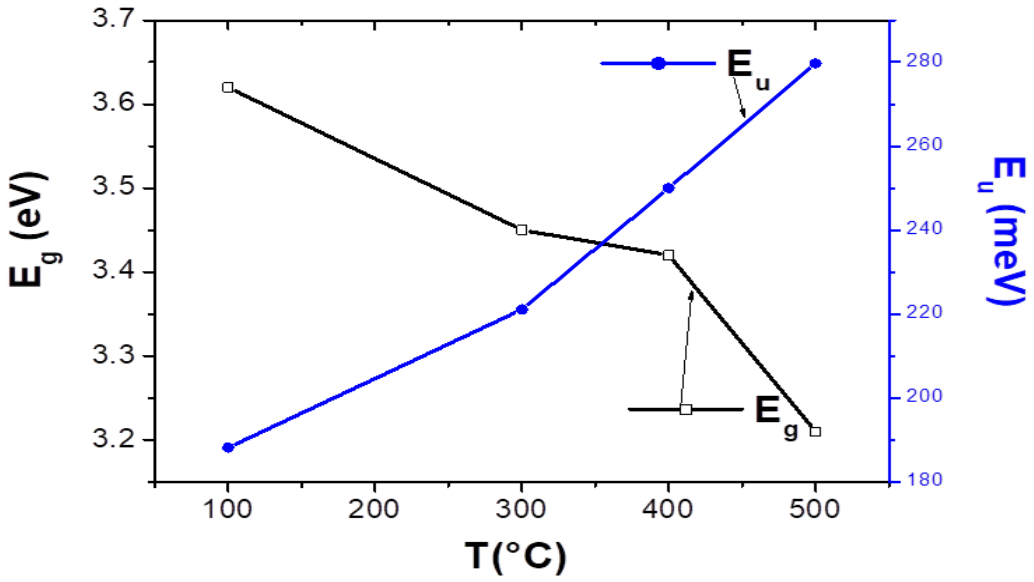


Figure III.8 Variations in the gap and disorder as a function of the annealing temperature for TiO2 films.

Figure III.8 shows the variation of the optical gap and that of disorder for the TiO_2 thin films prepared at different annealing temperatures; the optical gap and disorder vary inversely. From this, we observe that the optical gap in our thin films is governed by disorder.

Conclusion

Conclusion

In this work, the economical and adaptable sol-gel process was effectively used to create titanium dioxide (TiO_2) thin films on glass substrates at room temperature. The films were subjected to post-thermal annealing treatments for one hour at temperatures between 300°C and 500°C after deposition.

A combination of X-ray diffraction (XRD), atomic force microscopy (AFM), and ultraviolet-visible (UV-Vis) spectroscopy was used to conduct a thorough examination into the impacts of this thermal processing on the structural, morphological, and optical features.

The following is a summary of the study's main conclusions and revelations:

- **Structural Evolution**: as-deposited TiO_2 thin films have an amorphous structure at first, according to quantitative XRD measurements. Thermal annealing, on the other hand, causes a clear, irreversible phase transformation that greatly enhances the crystalline quality and encourages the exclusive growth of the active anatase phase between 300 and 500°C.

- **Surface Morphology**: AFM topography scans showed that surface roughness changed noticeably with temperature. The XRD results of improved atomic rearrangement and increased crystallinity were supported by the root-mean-square roughness, which rose with increasing annealing temperatures. The annealed films did, however, retain a non-negligible surface roughness (averaging 3.24 nm), which offers a high effective surface area that is very advantageous for surface-driven applications.

- **Optical Performance:** All synthetic films show outstanding, high transparency over the visible spectrum, according to UV-Vis spectrophotometry. Additionally, as the annealing temperature increased, a systematic shrinking of the optical bandgap was noted, with values ranging from 3.21 to 3.62 eV and at the same time the disorder increases. These energy gap estimates are in good agreement with published anatase TiO_2 literature data.

In conclusion, these results unequivocally demonstrate that post-deposition thermal annealing serves as an effective technique to correctly control and enhance the structural and optical properties of sol-gel produced TiO_2 thin films.

The integration of exceptional visual transparency, variable band gap energy, and a stable anatase crystalline structure offers these generated films as very intriguing prospects for advanced technological applications, especially in photocatalysis, optical waveguides, and optoelectronic devices.

REFERENCES

REFERENCES

[1] Nanotechnology and Photocatalysis for Environmental Applications, part of series: Micro and Nano Technologies, 2020.

[2] M. Khechba, Elaboration et étude des couches minces d'oxyde d'étain, Thèse de Doctorat, Université des Frères Mentouri-Constantine, Algérie, 2018.

[3] F. Ynineb, Contribution à l'élaboration de couches minces d'Oxydes Transparents Conducteurs (TCO), Thèse de Magister, Université des Frères Mentouri-Constantine, Algérie, 2010.

[4] F. Khelfaoui, Etude du mécanisme de croissance des couches a-Si:H élaborées par pulvérisation cathodique : interaction plasma-substrat, Ph.D. dissertation, Dépt. Physique, Univ. Frères Mentouri Constantine, Constantine, Algeria, 2014.

[5] R. Messemche, Elaboration and Characterization of Undoped and Doped Titanium Dioxide Thin Layers by Sol-Gel (Spin Coating) for Photocatalytic Applications, Ph.D. dissertation, University Mohamed Khider of Biskra, Biskra, Algeria, 2021.

[6] Y. Benkhetta, Elaboration and Characterization of Thin Layers of Zinc Oxide (ZnO) Deposited by Ultrasonic Spray for Photovoltaic and Optoelectronic Applications, Ph.D. dissertation, University Mohamed Khider of Biskra, Biskra, Algeria, 2019.

[7] K. Wasa, M. Kitabatake, and H. Adachi, Thin Film Materials Technology: Sputtering of Compound Materials, 2004.

[8] B. Lewis and J. C. Anderson, Nucleation and Growth of Thin Films. New York: Academic Press, 1978.

[9] D. Ulrike et al. "The Surface Science of Titanium Dioxide", Surface Science, Vol. 48, p. 67, 2003.

[10] Y. F. Zhang et al., "A Theoretical Study on the Electronic Structures of TiO_2: Effect of Hartree-Fock Exchange", The Journal of Physical Chemistry, Vol. 109, no. 41, p. 19271, 2005.

[11] P. Kelly and R. Arnell, "Magnetron Sputtering: A Review of Recent Developments and Applications", Vacuum, Vol. 56, pp. 159–172, 2000.

[12] P. Kelly, R. Arnell, and W. Ahmed, "Some Recent Applications of Materials Deposited by Unbalanced Magnetron Sputtering", Surface Engineering, Vol. 9, pp. 287–292, 1993.

[13] P. Martin, Introduction to Surface Engineering and Functionally Engineered Materials. John Wiley & Sons, 2011.

[14] S. Ricciardi, Surface Chemical Functionalization Based on Plasma Techniques. Lambert Academic Publishing, 2012.

[15] K. L. Chopra, Thin Film Phenomena. New York: Robert E. Krieger Publishing Co. Inc., 1979.

[16] J. George, Preparation of Thin Films. New York: Marcel Dekker Inc., 1992.

[17] A. Antony, Preparation and Characterisation of Certain II-VI, I-III-VI_2 Semiconductor Thin Films and Transparent Conducting Oxides, Ph.D. dissertation, Cochin University of Science and Technology, Cochin, Kerala, India, 2004.

[18] Y. G. Yushkov, E. M. Oks, A. V. Tyunkov, and D. B. Zolotukhin, " Dielectric Coating Deposition Regimes during Electron-Beam Evaporation of Ceramics in the Fore-Vacuum Pressure Range", Coatings, Vol. 12, no. 2, Art. no. 130, Jan. 2022.

[19] K. L. Chopra, Thin Film Phenomena. New York: Robert E. Krieger Publishing Co. Inc., 1979.

[20] L. Holland, Vacuum Deposition of Thin Films. New York: John Wiley & Sons Inc, 1956.

[21] M. C. Sharma, B. Tripathi, S. Kumar, S. Srivastava, and Y. K. Vijay, “Low Cost $CuInSe_2$ Thin Films Production by Stacked Elemental Layers Process for Large Area Fabrication of Solar Cell Application,” Materials Chemistry and Physics, Vol. 131, no. 3, pp. 600–604, 2012.

[22] M. Dahnoun, Preparation and Characterization of Titanium Dioxide and Zinc Oxide Thin Films via Sol-Gel (Spin Coating) Technique for Optoelectronic Applications, Ph.D. dissertation, University Mohamed Khider of Biskra, Algeria, 2020.

[23] J. Asim, M. Sh. Abdel-Wahab, and H. Ahmed Hosny, "Advance Deposition Techniques for Thin Film and Coating", IntechOpen, Vol. 2, no. 3, pp. 138–147, 2017.

[24] J. Carlsson and P. M. Martin, "Chemical Vapor Deposition", in Handbook of Deposition Technologies for Films and Coatings: Science, Applications and Technology, 3rd ed, Boston: William Andrew Publishing, pp. 314–363, 2010.

[25] H. M. M. Albetran, Synthesis and Characterisation of Nanostructured TiO_2 for Photocatalytic Applications, PhD Thesis, Curtin University, 2016.

[26] R. Pessoa, M. Fraga, L. Santos, et al., "Nanostructured Thin Films Based on TiO_2 and/or Sic for Use in Photo electrochemical Cells: A Review of the Material Characteristics, Synthesis and Recent Applications", Materials Science in Semiconductor Processing, Vol. 29, pp. 56–68, 2015.

[27] S. Kommu, G. M. Wilson, and B. Khomami, "A Theoretical/Experimental Study of Silicon Epitaxy in Horizontal Single-Wafer Chemical Vapor Deposition Reactors", Journal of the Electrochemical Society, Vol. 147, pp. 1538–1550, 2000.

[28] H. Pedersen and S. D. Elliott, "Studying Chemical Vapor Deposition Processes with Theoretical Chemistry", Theoretical Chemistry Accounts, Vol. 133, p. 1476, 2014.

[29] A. Ashour, M. A. Kaid, N. Z. El-Sayed, and A. A. Ibrahim, "Physical Properties of ZnO Thin Films Deposited by Spray Pyrolysis Technique", Applied Surface Science, Vol. 252, no. 22, pp. 7844–7848, 2006.

[30] A. Sanchez-Juarez, A. Tiburcio-Silver, and A. Ortiz, "Properties of Fluorine-Doped ZnO Deposited onto Glass by Spray Pyrolysis", Solar Energy Materials and Solar Cells, Vol. 52, no. 3–4, pp. 301–311, 1998.

[31] C. J. Brinker and S. W. Scherer, Sol-Gel Science: The Physics and Chemistry of Sol-Gel Processing. New York: Academic Press, 1990.

[32] B. Romain, Couches Minces d'Oxydes Élaborées par Voie Sol-Gel, Épitaxiées et Nanostructurées par Traitements Thermiques Post-Dépôt, Thèse de Doctorat, Université de Limoges, 2006.

[33] O. Tari, Sol-Gel Synthesis and Characterisation of Pure and Doped Transparent and Conductive ZnO Thin Films, Thèse de Doctorat, University of Naples Federico II, 2013.

[34] L. Yang, Fabrication and Characterization of Micro lasers by the Sol-Gel Method, PhD Thesis, California Institute of Technology, Pasadena, California, USA, 2005.

[35] E. Marenna, Sol-Gel Synthesis of Functional Nanocomposites Based on Inorganic Oxides, PhD Thesis, University of Naples Federico II, Italia, 2008.

[36] R. S. Devan, R. A. Patil, J.-H. Lin and Y.-R. Ma, "One-Dimensional Metal-Oxide Nanostructures: Recent Developments in Synthesis, Characterization, and Applications", Vol. 22, no. 16, 2012.

[37] M. Bathat, Thèse de Doctorat, Université Claude Bernard Lyon 1, 1992.

[38] L. Nadar, Surfaces fonctionnalisées à base de nanoparticules métalliques pour l'optique et la photonique, PhD thesis, Jean Monnet University, Saint-Étienne, France, 2011.

[39] A. Yahia, Optimization of Indium Oxide Thin Films Properties Prepared by Sol-Gel Spin Coating Process for Optoelectronic Applications, Thèse de Doctorat, University of Biskra, 2020.

[40] L. E. Scriven, C. J. Brinker, D. E. Clark, and D. R. Ulrich, Better Ceramics Through Chemistry III, Materials Research Society, 1988.

[41] C. J. Brinker, A. J. Hurd, G. C. Frye, P. R. Schunk, and C. S. Ashley, "Sol-Gel Thin Film Formation", Journal of the Ceramic Society of Japan, Vol. 99, pp. 862–877, 1991.

[42] Y. Yun, Recent Advances in Carbon Capture and Storage. Intech Open, 2017.

[43] M. J. Gázquez et al, "A Review of the Production Cycle of Titanium Dioxide Pigment", Materials Sciences and Applications, Vol. 5, p. 441, 2014.

[44] K. G. Budinski, Surface Engineering for Wear Resistance. Prentice-Hall, Englewood Cliffs, New Jersey, USA, 1988.

[45] M. J. Gázquez, J. P. Bolivar, R. Garcia-Tenorio, and F. Vaca, "A Review of the Production Cycle of Titanium Dioxide Pigment", Materials Sciences and Applications, Vol. 5, no. 7, pp. 441–458, 2014.

[46] N. Rahimi, R. A. Pax, and E. M. Gray, "Review of Functional Titanium Oxides. I: TiO_2 and Its Modifications", Progress in Solid State Chemistry, 2016.

[47] Q. Deng, Band Gap Tuning and Structural Engineering of TiO_2 for Photocatalysis and Solar Cells, Thèse de Doctorat, University of Bolton, 2012.

[48] V. Etacheri, C. D. Valentin, J. Schneider, D. Bahnemann, and S. C. Pillai, " Visible-Light Activation of TiO_2 Photocatalysts: Advances in Theory and Experiments", Journal of Photochemistry and Photobiology C: Photochemistry Reviews, Vol. 25, pp. 13–29, 2015.

[49] S. D. Mo and W. Y. Ching, "Electronic and Optical Properties of Three Phases of Titanium Dioxide: Rutile, Anatase, and Brookite", Physical Review B, Vol. 51, no. 1, 1995.

[50] A. A. Gribb and J. F. Banfield, "Particle Size Effects on Transformation Kinetics and Phase Stability in Nanocrystalline TiO_2", American Mineralogist, Vol. 82, pp. 717–728, 1997.

[51] H. Zhang and J. F. Banfield, "Thermodynamic Analysis of Phase Stability of Nanocrystalline Titania", Journal of Materials Chemistry, Vol. 8, pp. 2073–2076, 1998.

[52] M. R. Ranade et al., "Energetics of Nanocrystalline TiO_2", Vol. 99, pp. 2–7, 2002.

[53] S. J. Smith et al, " Heat Capacities and Thermodynamic Functions of TiO_2 Anatase and Rutile: Analysis of Phase Stability", American Mineralogist, Vol. 91, pp. 91–91, 2009.

[54] I. Cimieri, Sol-Gel Preparation and Characterization of Titanium Dioxide Films for Degradation of Organic Pollutants, Ph.D. dissertation, Faculty of Sciences, Ghent University, Ghent, Belgium, 2014.

[55] F. Trabelsi, Sol-Gel/ALD Low Temperature Process: Study of Al_2O_3 and Codoped TiO_2 Nanostructures for Photovoltaic Applications, Ph.D. dissertation, Université Grenoble Alpes and Université de Sfax, 2021.

[56] B. Zheng, Q. Guo, D. Wang, H. Zhang, Y. Zhu, and S. Zhou, "Energy-Transfer Modulation for Enhanced Photocatalytic Activity of Near-Infrared Up conversion Photocatalyst", Journal of the American Ceramic Society, Vol. 98, no. 1, pp. 1363–140, 2015.

[57] F. Huang, A. Yan, and H. Zhao, "Influences of Doping on Photocatalytic Properties of TiO_2 Photocatalyst", Semiconductor Photocatalysis - Materials, Mechanisms and Applications, 2016.

[58] B. Thomas, Des Nanotitanates de Sodium aux Dioxydes de Titane: Électrode Négative à Base de TiO_2 (B) Nanométrique pour Accumulateur Lithium Ion, Thèse de Doctorat, Université de Nantes, France, 2009.

[59] S. Pardis, Synthèse de Nanoparticules d'Oxyde de Titane par Pyrolyse Laser: Étude des Propriétés Optiques et de la Structure Électronique, Thèse de Doctorat, Université Paris Sud XI, France, 2001.

[60] B. S. Richards, Novel Uses of Titanium Dioxide for Silicon Solar Cells, Ph.D. dissertation, University of New South Wales, Sydney, NSW, Australia, 2002.

[61] M. E. Kurtoglu, T. Longenbach, K. Sohlberg, and Y. Gogotsi, "Strong Coupling of Cr and N in Cr-N-Doped TiO_2 and Its Effect on Photocatalytic Activity", The Journal of Physical Chemistry C, Vol. 115, no. 35, pp. 17392–17399, 2011.

[62] T. Luttrell, S. Halpegamage, J. Tao, A. Kramer, E. Sutter, and M. Batzill, "Why Is Anatase a Better Photocatalyst than Rutile? Model Studies on Epitaxial TiO_2 Films", Scientific Reports, Vol. 4, no. 1, pp. 1–8, 2014.

[63] E. E. Ebrahiem, H. A. A. Farag, M. Y. Ghaly, and R. A. Mohamed, "Treatment of Oily Wastewater Using Advanced Solar Photo-Catalytic Oxidation Process Using Titanium Dioxide Doped Nano Fibers", Egyptian Journal of Chemistry, Vol. 65, no. 7, pp. 479–488, Jul. 2022.

[64] M. I. Litter, Applied Catalysis B: Environmental, Vol. 23, pp. 89–114, 1999.

[65] A. Bahtat, M. Bouderbala, M. Bahtat, M. Bouazaoui, J. Mugnier, and M. Druetta, Thin Solid Films, Vol. 323, p. 59, 1998.

[66] A. Verma, A. Basu, A. K. Bakhshi, and S. A. Agnihotry, Solid State Ionics, Vol. 176, p. 228, 2005.

[67] M. BOUSSOUM OuizaElaboration et Étude des Propriétés des Couches Minces d'Oxydes et de Nanocomposites à Base de TiO_2. memoire de magister 2011

Université Mouloud Mammeri de Tizi-Ouzou

[68] W. Rahmalia, Paramètres de performances de photo-électrodes de TiO_2/Kaolinite et d'électrolytes à base de carbonates biosourcés dans la cellule solaire sensibilisée par la bixine, Ph.D. dissertation, Université de Toulouse, Toulouse, France, 2016.

[69] M. Landmann, E. Rauls and W. G. Schmidt, "The electronic structure and optical response of rutile, anatase and brookite TiO2", J. Phys. Condens. Matter Vol. 24, no. 19, pp. 195503, 2012.

[70] P. Charles and Jr. Poole, Encyclopedic Dictionary of Condensed Matter Physics, Vol. 1, Department of Physics and Astronomy, University of South Carolina, Columbia, SC, USA, 2004.

[71] O. Noguera, Propriétés Structurales, Vibrationnelles et Diélectriques de Matériaux à Base d'Oxyde de Tellure, Ph.D. dissertation, Université de Limoges, Limoges, France, 2003.

[72] A. W. Van Herwaarden and P. M. Sarro, Sensors Actuat, Vol. 10, p. 321, 1986.

[73] D.B. M. Hoffman. S. Martin. W. Choi, "Environmental applications of semiconductor photocatalysis", Chemical Reviews, vol. 95, no. 1, pp. 69-96, 1995.

[74] C. R. Brundle, L. Wilson, C. A. Evans, S. Wilson, and G. Wilson, Encyclopedia of Materials Characterization Surface, Interface, Thin Films, Gulf Professional Publishing, USA, 1992.

[75] M. Devika and K. T. R. Reddy, Applied Physics, Vol. 100, p. 023518, 2006.

[76] H. Yilmazer, M. Niinomi, T. Akahori, M. Nakai, and Y. Todaka, "Effect of high-pressure torsion processing on microstructure and mechanical properties of a novel biomedical β-type Ti-29Nb-13Ta-4.6Zr after cold rolling," International Journal of Microstructure and Materials Properties, vol. 7, no. 2–3, pp. 168–186, 2012.

[77] S. P. Choudhury et al., Materials Today: Proceedings, Vol. 3, pp. 1609–1619, 2016.

[78] F. Mahcene, Synthèse par Sol-gel et caractérisation structurale et optique de nano poudres de ZnO pures et dopées en Aluminium (0.1, 0.5, 0.75, 1.5 - 7, 10, 15 et 20 % at)", Doctorat en Sciences, Spécialité: Sciences des Matériaux, Université Mentouri Constantine 1, Algérie, 2021.

[79] A. Adjimi, Elaboration des oxydes transparents conducteurs par voie sol-gel, Doctorat, Université Frères Mentouri Constantine1, 2021.

[80] O. Beldjebli, Élaboration et caractérisation des matériaux pour la photocatalyse obtenus par la voie sol-gel, PhD dissertation, Université Frères Mentouri-Constantine 1, Algérie, 2021.

[81] N. Boukhenoufa, Contribution à l'Étude des Propriétés des Films Minces à Base de ZnO, PhD dissertation, Université de Batna 2, Algérie, 2017.

[82] D. Adnane, Caractéristiques optiques et structurales des couches minces d'oxyde de titane obtenues par voie Sol-Gel, Mémoire de Magister, Dépt. de Physique, Univ. Mentouri Constantine, Constantine, Algeria, 2005.

[83] F. Saker, Préparation et caractérisation de couches minces d'oxyde de zinc (ZnO) et de couple d'oxydes, Mémoire de Magister, Université des Frères Mentouri – Constantine 1, 2014.

[84] S. Rahmane, M. S. Aida, M. A. Djouadi, and N. Barreau, "Effects of thickness variation on properties of ZnO:Al thin films grown by RF magnetron sputtering deposition," Superlattices and Microstructures, Vol. 79, pp. 148-155, Mar. 2015.

[85] R. Mechiakh and R. Bensaha, "Variation of the Structural and Optical Properties of Sol-Gel TiO_2 Thin Films with Different Treatment Temperatures", C. R. Phys., Vol. 7, pp. 464–470, 2006.

[86] B. D. Cullity, Elements of X-Ray Diffraction, 2nd ed. Reading: Addison-Wesley, 1978.

[87] F. Huang, H.-Z. Zhang, and J. F. Banfield, "Two-Stage Crystal-Growth Kinetics Observed During Hydrothermal Coarsening of Nanocrystalline ZnS", Nano Letters, Vol. 3, pp. 373–378, 2003.

[88] N. Ibrahim, S. Al-Shomar, and S. Ahmad, "Effect of Annealing Temperature on the Structural and Optical Properties of Nanocrystalline ZnO Thin Films Prepared by Sol-Gel Method", Sains Malaysiana, Vol. 42, no. 12, pp. 1781–1786, 2013.

[89] Y. Q. Hou, D. M. Zhuang, G. Zhang, and M. Zhao, "Influence of Annealing Temperature on the Properties of Titanium Oxide Thin Film", Applied Surface Science, Vol. 218, pp. 98–106, 2003.

[90] A. R. A. Rashid and H. K. Tazri, "Optical Properties of ZnO, TiO_2 and ZnO:TiO_2 Composite Films", Nano Hybrids and Composites, Vol. 31, pp. 25–33, 2021.

[91] W. Weng, M. Ma, P. Du, G. Zhao, G. Shen, J. Wang, and G. Han, "Superhydrophilic Fe Doped Titanium Dioxide Thin Films Prepared by a Spray Pyrolysis Deposition", Surface and Coatings Technology, Vol. 198, pp. 340–344, 2005.

[92] D. J. Kim, S. H. Hahn, S. H. Oh, and E. J. Kim, Materials Letters, Vol. 57, p. 355, 2002.

[93] H. Tang, H. Berger, P. E. Schmid, F. Lévy, "Optical properties of anatase (TiO_2)," Solid State Communications, Vol. 92, no. 3, pp. 267-271, 1994.

[94] F. M. El-Hossary, S. H. Mohamed, E. A. El-Kassem Noureldein, and M. A, "Influence of RF Power on Growth, Structural and Optical Properties of ZnO Synthesized via Vapor Transport in Inductively Coupled Plasma", Materials Science in Semiconductor Processing, Vol. 120, p. 105284, 2020.